

1 **Contribution of expanded marine sulfur chemistry to the seasonal variability
2 of DMS oxidation products and size-resolved sulfate aerosol**

3 Linia Tashmim¹, William C. Porter¹, Qianjie Chen², Becky Alexander³, Charles H. Fite⁴,
4 Christopher D. Holmes⁴, Jeffrey R. Pierce⁵, Betty Croft⁶, and Sakiko Ishino⁷

5 ¹Department of Environmental Sciences, University of California, Riverside, CA, USA

6 ²Department of Civil and Environmental Engineering, The Hong Kong Polytechnic University,
7 Hong Kong, China

8 ³Department of Atmospheric Sciences, University of Washington, Seattle, WA, USA

9 ⁴Department of Earth, Ocean and Atmospheric Science, Florida State University, Tallahassee,
10 FL, USA

11 ⁵Department of Atmospheric Science, Colorado State University, Fort Collins, CO, USA

12 ⁶Department of Physics and Atmospheric Science, Dalhousie University, Halifax, Nova Scotia,
13 Canada

14 ⁷Institute of Nature and Environmental Technology, Kanazawa University, Japan

15 Correspondence: Linia Tashmim (ltash001@ucr.edu) and William C. Porter
16 (william.porter@ucr.edu)

17 **Abstract.** Marine emissions of dimethyl sulfide (DMS) and the subsequent formation of its
18 oxidation products methane sulfonic acid (MSA) and sulfuric acid (H_2SO_4) are well-known natural
19 precursors of atmospheric aerosols, contributing to particle mass and cloud formation over ocean
20 and coastal regions. Despite a long-recognized and well-studied role in the marine troposphere,
21 DMS oxidation chemistry remains a work in progress within many current air quality and climate
22 models, with recent advances exploring heterogeneous chemistry and uncovering previously
23 unknown intermediate species. With the identification of additional DMS oxidation pathways and
24 intermediate species influencing its eventual fate, it is important to understand the impact of these
25 pathways on the overall sulfate aerosol budget and aerosol size distribution. In this work, we
26 update and evaluate the DMS oxidation mechanism of the chemical transport model GEOS-Chem
27 by implementing expanded DMS oxidation pathways into the model. These updates include gas-
28 and aqueous-phase reactions, the formation of the intermediates dimethyl sulfoxide (DMSO) and
29 methane sulphonic acid (MSIA), as well as cloud loss and aerosol uptake of the recently quantified
30 intermediate hydroperoxymethyl thioformate (HPMTF). We find that this updated mechanism
31 collectively decreases the global mean surface-layer gas-phase sulfur dioxide (SO_2) mixing ratio
32 by ~~40%~~ and enhances sulfate aerosol (SO_4^{2-}) mixing ratio by ~~17%~~. We further perform sensitivity
33 analyses exploring the contribution of cloud loss and aerosol uptake of HPMTF to the overall
34 sulfur budget. Comparing modeled concentrations to available observations we find improved
35 biases relative to previous studies. To quantify impacts of these chemistry updates on global
36 particle size distributions and mass concentration we use the TOMAS aerosol microphysics
37 module coupled to GEOS-Chem, finding changes in particle formation and growth affect the size
38 distribution of aerosol. With this new DMS-oxidation scheme the global annual mean surface layer
39 number concentration of particles with diameters smaller than 80 nm decreases by ~~16.8%~~, with
40 cloud loss processes related to HPMTF mostly responsible for this reduction. However, global
41 annual mean number of particles larger than 80 nm increases by ~~3.8%~~ suggesting that the new
42 scheme promotes seasonal particle growth to these sizes capable of acting as cloud condensation
43 nuclei (CCN).

Deleted: 35

Deleted: 22

Deleted: 12

Deleted: 1%,

48

1 Introduction

49 Dimethyl sulfide (DMS: CH_3SCH_3) is the most abundant biological source of sulfate aerosol and
50 has a significant influence on Earth's radiation budget and climate due to its contribution to
51 atmospheric marine particle (Charlson et al., 1987; Fung et al., 2022). In the atmosphere, DMS
52 reacts with hydroxyl radical (OH), nitrate radical (NO_3), ozone (O_3) and various halogen species
53 (e.g., chlorine (Cl) and bromine oxide (BrO)), primarily forming sulfur dioxide (SO_2) and methyl
54 sulfonic acid (MSA: $\text{CH}_3\text{SO}_3\text{H}$) (Chen et al., 2018; Falloona, 2009; Hoffmann et al., 2016). These
55 oxidation products are considered key influences on the formation and evolution of natural
56 aerosols and clouds along with their associated climate impacts, especially in the marine boundary
57 layer (MBL) (Carslaw et al., 2013; Sipilä et al., 2010; Schobesberger et al., 2013; Thomas et al.,
58 2010; von Glasow and Crutzen, 2004). SO_2 and MSA formed by DMS oxidation can be deposited
59 on Earth surface or further oxidize affecting the size distribution of aerosol and cloud microphysics
60 (Leaitch et al., 2013; Wollesen de Jonge et al., 2021). SO_2 can either oxidize in the gas-phase by
61 reaction with the OH radical forming H_2SO_4 , which can participate in nucleation and early growth
62 of particles in the atmosphere, or it can be taken up by cloud droplets and undergo aqueous phase
63 oxidation by reaction with H_2O_2 , O_3 and O_2 catalyzed by transition metals (Mn, Fe) forming SO_4^{2-}
64 and generally only contributing to the growth of aerosol particles (Hoyle et al., 2016; Kulmala,
65 2003; Alexander et al., 2009). The hypohalous acids (HOBr, HOCl, HOI) also plays significant
66 role in aqueous-phase sulfate production in the marine boundary layer (MBL) (Chen et al., 2016;
67 Sherwen et al., 2016b). Recent studies have highlighted the importance of natural aerosols
68 originating from DMS oxidation and their contribution to the uncertainty of aerosol radiative
69 forcing in climate models (Carslaw et al., 2013; Fung et al., 2022; Rosati et al., 2022; Novak et al.,
70 2021, 2022). Since DMS-derived aerosol is a major source of uncertainty in estimating the global
71 natural aerosol burden and associated aerosol indirect radiative forcing, a more accurate
72 representation of DMS oxidation and particle formation processes is an important step towards
73 improved Earth system and climate modeling.

74 Although the chemistry of DMS oxidation has been previously studied in great detail, known
75 uncertainties and omissions in the current mechanism remain in current air quality and chemical
76 transport models (Barnes et al., 2006; Fung et al., 2022; Hoffmann et al., 2016, 2021). Furthermore,
77 while increasingly complex and experimentally validated mechanisms are under ongoing
78 development, DMS oxidation processes in many current chemical transport models continue to be
79 represented through simplified gas-phase reactions with the tropospheric oxidants OH and NO_3 ,
80 producing the two major oxidation products SO_2 and MSA at a fixed ratio as shown in R1-R3 in
81 Table 1 (Chen et al., 2018; Chin et al., 1996; Veres et al., 2020). This type of simplified mechanism
82 neglects the formation and loss of important intermediates such as dimethyl sulfoxide (DMSO:
83 CH_3SOCH_3), methane sulphinic acid (MSIA: $\text{CH}_3\text{SO}_2\text{H}$) and the recently discovered oxidation
84 product hydroperoxymethyl thioformate (HPMTF: $\text{HOOCH}_2\text{SCHO}$) (Berndt et al., 2019; Veres et
85 al., 2020; Wu et al., 2015; Khan et al., 2021).

86 These omissions can have major consequences on product yields of DMS oxidation, thereby
87 affecting the aerosol burdens. For example, the OH -addition pathway of DMS forms DMSO and
88 MSIA as the intermediates, which has been identified as a dominant source of MSA via their
89 aqueous-phase oxidation, and a fraction of that MSA subsequently undergoes aqueous-phase
90 oxidation to form sulfate aerosol (Chen et al., 2018; Ishino et al., 2021; Zhu et al., 2006; von
91 Glasow and Crutzen, 2004). Previous studies suggest that BrO contributes to 8 – 30% of total DMS

Deleted: ;

loss, highlighting the importance of this pathway as well (Breider et al., 2010; Boucher et al., 2003; Chen et al., 2018; Khan et al., 2016). More recent experimental and laboratory studies have confirmed the formation of methylthiomethyl peroxy radicals ($\text{CH}_3\text{CH}_2\text{OO}$; abbreviated as MSP or MTMP) from the H-abstraction channel of OH oxidation, which can subsequently lead to a series of rapid intramolecular H-shift isomerization reactions, ultimately resulting in the formation of the stable intermediate HPMTF (Berndt et al., 2019; Veres et al., 2020; Vermeuel et al., 2020; Wu et al., 2015; Fung et al., 2022; Jernigan et al., 2022a). It has been reported that 30–46% of emitted DMS forms HPMTF according to different modeling studies and this falls within the observational range from NASA Atmospheric Tomography ATom-3 and ATom-4 flight campaigns where about 30–40% DMS was oxidized to HPMTF along their flight tracks (Fung et al., 2022; Veres et al., 2020; Novak et al., 2021). Subsequent investigation of the isomerization rate and heterogeneous loss of HPMTF in cloud droplets and aerosol shows a high production rate of marine carbonyl sulfide (OCS) from the chemical loss of HPMTF, a potential precursor of stratospheric sulfate aerosol and significant inhibitor of cloud condensation nuclei (CCN) formation due to the resulting reduction of surface SO_2 (Jernigan et al., 2022a). With the latest experimental findings on heterogeneous loss process of HPMTF and experimentally validated oxidation reactions for OCS formation directly from HPMTF it is necessary to include these reactions as part of the DMS oxidation mechanism as these will have impact on overall yield of SO_2 , thus affecting the formation probability of CCN (Jernigan et al., 2022a, b).

Table 1. The three DMS oxidation reactions in the standard GEOS-Chem chemical mechanism

Reactions	Rate constant ($\text{cm}^3 \text{molecule}^{-1} \text{s}^{-1}$)
$\text{DMS} + \text{OH}_{(\text{abstraction})} \rightarrow \text{SO}_2 + \text{CH}_3\text{O}_2 + \text{CH}_2\text{O}$	$1.20 \times 10^{-11} \exp(-280/T)$ (R1)
$\text{DMS} + \text{OH}_{(\text{addition})} \rightarrow 0.75 \text{SO}_2 + 0.25 \text{MSA} + \text{CH}_3\text{O}_2$	$8.2 \times 10^{-39} [\text{O}_2] \exp(5376/T) / (1 + 1.05 \times 10^{-5} [\text{O}_2] / [\text{M}])$ (R2)
$\text{DMS} + \text{NO}_3 \rightarrow \text{SO}_2 + \text{HNO}_3 + \text{CH}_3\text{O}_2 + \text{CH}_2\text{O}$	$1.90 \times 10^{-13} \exp(530/T)$ (R3)

Considering these and other consequences of complex DMS oxidation processes, a heavily simplified oxidation scheme will necessarily neglect potentially important reaction intermediates along with their production and loss pathways, with implications for the concentration and distribution of the oxidation products, including particulate sulfate. Differing intermediate lifetimes further influence sulfur removal and transport depending on the relative dominance of pathways. Thus, the exclusion of key pathways and intermediate species can lead to errors in the representation of the spatial distribution of both gas- and particle-phase sulfur species, as well as global sulfur burden.

The DMS oxidation products sulfate and MSA play an important role in Earth's radiative budget through cloud droplet formation, and the extent of this role depends on how efficiently they can produce and grow new particles in the marine atmosphere (Thomas et al., 2010). SO_2 can oxidize in the gas-phase forming H_2SO_4 , which acts as a key product contributing to nucleation and condensational growth as shown in Figure 1. SO_2 oxidizing through aqueous chemistry in cloud droplets does contribute to particle growth rates by providing larger aerosol during cloud evaporation that acts as more efficient CCN (Kaufman and Tanré, 1994). On the other hand, MSA might participates in nucleation along with sulfuric acid in presence of amines or ammonia (Johnson and Jen, 2023). Recent studies have highlighted the importance of aqueous-phase chemistry in the formation and loss of MSA (Boniface et al., 2000; Chen et al., 2015; Kaufman and Tanré, 1994; Kulmala et al., 2000).

Deleted: (

Deleted: -

Formatted: Font: Not Bold,

Formatted: Font: Not Bold,

Formatted Table

Deleted: $20e-11 * \exp$

Deleted: e^{5376}

Deleted: $/$

Formatted: Not Superscript/ Subscript

Formatted: Subscript

Deleted: e^{3644}

Deleted: $) \text{ cm}^3 \text{molecule}^{-1} \text{s}^{-1}$

Formatted: Not Superscript/ Subscript

Deleted: $90e-13 * \exp$

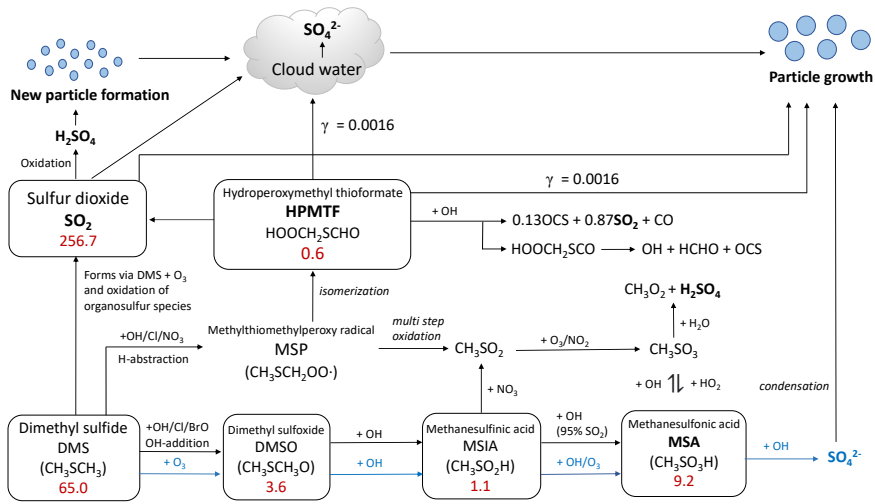
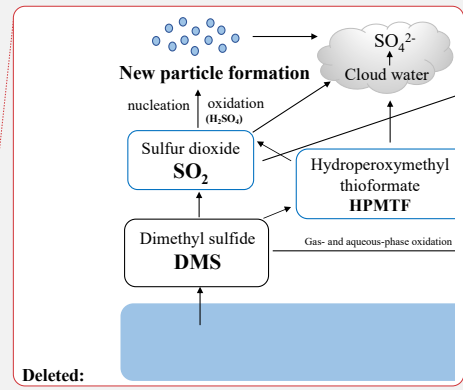


Figure 1 Modified DMS oxidation mechanism used in this work (simulation MOD) showing the formation of major stable oxidation products (**in bold**) including the newly identified intermediate HPMTF, and their contribution to new particle formation or growth of existing particles. The blue arrows and text represent aqueous-phase reactions. Numbers inside boxes indicate burden in units of PgS . γ values represent reactive uptake coefficients for heterogeneous loss of HPMTF to cloud and aerosol. Note that SO₂ formation from DMS and HPMTF involves multiple oxidation steps in this mechanism, but full pathways are simplified here for visual clarity.



142 Additionally, the recently identified intermediate HPMTF also has the potential for further gas-
143 phase oxidation. Under cloud-free conditions, HPMTF can undergo gas-phase oxidation by OH,
144 producing SO₂ and eventually leading to the formation of non-sea-salt-SO₄²⁻. This sulfate can
145 contribute to aerosol formation and growth processes, with climate implications (Galí et al., 2019).
146 Other work has used direct airborne eddy covariance flux measurements to explain the chemical
147 fate of HPMTF in the MBL, finding that in cloudy conditions chemical loss due to aqueous phase
148 reactions in clouds is the major HPMTF removal process (Novak et al., 2021). In the same study,
149 global model simulations showed a 35% reduction in global annual average SO₂ production from
150 DMS and a 24% reduction in the near-surface (0 to 3 km) global annual average SO₂
151 concentrations over the ocean as a result of this process (Novak et al., 2021). Thus, a complete
152 representation of cloud loss and aerosol uptake is needed to effectively evaluate the atmospheric
153 impacts of marine DMS and their connections to cloud formation (Novak et al., 2021; Holmes et
154 al., 2019).

155 To better understand the marine sulfur budget, as well as the eventual formation, size distribution,
156 and seasonality of sulfate aerosol, we use the global chemical transport model GEOS-Chem,
157 integrating previously developed mechanisms along with newly proposed pathways involving the
158 formation and loss of the intermediates DMSO, MSIA, and HPMTF. As part of this work, we
159 further quantify the atmospheric impacts of individual reactions and mechanisms, evaluate
160 uncertainties in the chemical mechanism, and identify improvements necessary to better represent
161 the impacts of DMS more accurately on atmospheric chemistry and climate. The resulting

175 integrated scheme provides a more complete representation of marine sulfur and sulfate aerosol
176 species in marine tropospheric environments compared to the simplified base GEOS-Chem
177 mechanism, with improved comparisons to aircraft and surface observations. Since aerosols are a
178 major contributor to uncertainty in climate forcing, improving oxidation and aerosol formation
179 mechanisms by adding and optimizing neglected reactions in models is a crucial step towards a
180 more mechanistically robust representation of particle yields and sensitivities. We further perform
181 multiple sensitivity tests to investigate how the uncertainty in heterogeneous uptake of the newly
182 identified HPMTF could influence DMS chemistry and tropospheric aerosol formation (Holmes
183 et al., 2019; Novak et al., 2021). In a broader sense our work provides a more detailed story on the
184 heterogeneous loss, fate, and ultimate impacts of DMS and its oxidation products, improving our
185 understanding of a key ocean-atmosphere interaction in the context of global change.

186 **2 Methodology**

187 To simulate DMS chemistry and its oxidation products GEOS-Chem global chemical transport
188 model v12.9.3 is used. Impacts on simulated aerosol size, number and mass concentration are
189 considered by coupling the Two-Moment Aerosol Sectional (TOMAS) aerosol microphysics
190 module with GEOS-Chem v12.9.3 (GC-TOMAS) (<https://github.com/geoschem/geoschem/tree/12.9.3>) (Adams and Seinfeld, 2002; Kodros and Pierce, 2017). The default GEOS-Chem
191 chemical mechanism contains detailed HO_x-NO_x-VOC-O₃-halogen tropospheric chemistry
192 along with recently updated halogen chemistry and in-cloud processing (Bey et al., 2001; Holmes
193 et al., 2019; Chen et al., 2017; Parrella et al., 2012; Schmidt et al., 2016; Wang et al., 2019). The
194 DMS emission flux from ocean are controlled by a gas transfer velocity which is dependent on sea
195 surface temperature and wind speed (Johnson, 2010) and a climatology of concentrations in
196 seawater (Lana et al., 2011; Nightingale et al., 2000). The aqueous-phase concentration of O₃ in
197 aerosols or cloud droplets is calculated assuming gas-liquid equilibrium and aqueous-phase
198 concentration of OH is calculated following [OH_(aq)] = δ[OH_(g)] where, δ = 1 × 10⁻¹⁹ M cm³
199 molecule⁻¹ (Jacob et al., 2005; Chen et al., 2018).

200 In this study, TOMAS tracks aerosol number and the mass of each aerosol species in 15
201 logarithmically sized bins, with sizes in this analysis ranging from 3 nm to 10 μm (Lee and Adams,
202 2012; Lee et al., 2013). All binned aerosol species undergo interactive microphysics, allowing the
203 calculation of aerosol number budgets (Westervelt et al., 2013). The version of GC-TOMAS used
204 here includes 47 vertical levels, a horizontal resolution of 4° × 5°, and the GEOS-FP data product
205 for meteorological inputs. Simulations are performed for 2018, with 11 months of discarded model
206 spin up. Nucleation is simulated via a ternary nucleation scheme involving water, sulfuric acid,
207 and ammonia with nucleation rates scaled by 10⁻⁵ (Napari et al., 2002; Westervelt et al., 2013). In
208 low-ammonia regions (less than 1 pptv), a binary nucleation scheme involving water and sulfuric
209 acid is instead used (Vehkamäki et al., 2002). Previously GC-TOMAS has been used for aerosol
210 simulations to investigate topics such as the aerosol cloud-albedo effect and cloud condensation
211 nuclei formation (Kodros et al., 2016; Kodros and Pierce, 2017; Pierce and Adams, 2006;
212 Westervelt et al., 2013). Aerosol species available for GC-TOMAS simulations are sulfate, aerosol
213 water, black carbon, organic carbon, mineral dust, and sea salt (Alexander et al., 2005; Bey et al.,
214 2001; Duncan Fairlie et al., 2007; Pye et al., 2009). The wet and dry deposition scheme for aerosols
215 and gas species are based on previous studies (Amos et al., 2012; Emerson et al., 2020; Liu et al.,
216 2001; Wesely, 1989; Wang et al., 1998).

217 We refer to simulations performed using only these three DMS oxidation reactions (Table 1) as
218 the “BASE”, involving only the direct formation of SO₂ and MSA in gas-phase (Chin et al., 1996).
219 We further implement and evaluate a custom chemical mechanism for DMS oxidation, referred to
220 as “MOD” (Table 2-4), representing an integration of three individual DMS oxidation mechanism
221 updates explored previously using GEOS-Chem and CAM6-Chem. This mechanism also includes
222 HPMTF loss to clouds and aerosols via heterogeneous chemistry, dry and wet deposition of
223 HPMTF, along with further improvement based on recent literature updates to chemical kinetics
224 (Chen et al., 2018; Fung et al., 2022; Veres et al., 2020; Novak et al., 2021; Cala et al., 2023). In
225 GC-TOMAS we use specific subroutine that take amount of sulfate produced via in-cloud
226 oxidation and condense it into an existing aerosol size distribution. So, mass of sulfate produced
227 by oxidation is portioned to the various size bins according to the number of particles in that size
228 bin. TOMAS microphysics accounts for H₂SO₄ formation based on gas-phase oxidation of SO₂

Deleted: , along with HPMTF loss via heterogenous chemistry in clouds and aerosols and dry and wet deposition of HPMTF (Chen et al., 2018; Fung et al., 2022; Veres et al., 2020; Novak et al., 2021). Loss of HPMTF in clouds follow entrainment-limited uptake which used a chemical rate expression to control rate of mixing between cloudy and clear air (Holmes et al., 2019).

Formatted

237 included in the kinetic preprocessor (KPP) equation list valid for the simulation BASE. Since there
 238 are additional sources of sulfate in the integrated DMS oxidation mechanism both in gas and
 239 aqueous phase, we made necessary changes in the KPP code to explicitly track H_2SO_4 formation
 240 by gas phase oxidation of SO_2 . On the other hand, code changes for sulfate formed by
 241 heterogeneous oxidation of MSA and HPMTF (in clouds and aerosols) were added in the GEOS-
 242 Chem microphysics module that also handles in-cloud oxidation of SO_2 in GC version 12.9.3 (Park
 243 et al., 2004; Trivitayanurak et al., 2008).

244 **Table 2.** Overview of the DMS oxidation mechanism via OH-addition pathway.

Gas-phase reactions	Rate constant ($cm^3\ molecule^{-1}\ s^{-1}$)	References
$DMS + OH \rightarrow DMSO + HO_2$	$9.5 \times 10^{-39} [O_2] \exp(5270/T) / (1 + 7.5 \times 10^{-29} [O_2] \exp(5610/T))$	JUPAC SOx22 (upd. 2006)
$DMS + BrO \rightarrow DMSO + Br$	$1.50 \times 10^{-14} \exp(1000/T)$	(Bräuer et al., 2013; Hoffmann et al., 2016)
$DMS + O_3 \rightarrow SO_2$	1.50×10^{-19}	(Du et al., 2007; Burkholder et al., 2020)
$DMSO + OH \rightarrow 0.95(MSIA + CH_3O_2)$	$6.10 \times 10^{-12} \exp(800/T)$	MCMv3.3.1. (von Glasow and Crutzen, 2004; Burkholder et al., 2020)
$MSIA + OH \rightarrow 0.95SO_2 + 0.95CH_3O_2$	9.00×10^{-11}	MCMv3.3.1
$MSIA + OH \rightarrow 0.05MSA + 0.05HO_2 + 0.05H_2O$	9.00×10^{-11}	(von Glasow and Crutzen, 2004)
$MSIA + NO_3 \rightarrow CH_3SO_2 + HNO_3$	1.00×10^{-13}	(von Glasow and Crutzen, 2004; Hoffmann et al., 2016)
Aqueous-phase reactions	$k_{298} [M^{-1}s^{-1}]$	References
$DMS (aq) + O_3 (aq) \rightarrow DMSO (aq) + O_2 (aq)$	8.61×10^8	(Gershenzon et al., 2001; Hoffmann et al., 2016)
$DMSO (aq) + OH (aq) \rightarrow MSIA (aq)$	6.65×10^9	(Zhu et al., 2003; Hoffmann et al., 2016)
$MSIA (aq) + OH (aq) \rightarrow MSA (aq)$	6.00×10^9	(Hoffmann et al., 2016; Herrmann et al., 1998)
$MSI^- (aq) + OH (aq) \rightarrow MSA (aq)$	1.20×10^{10}	(Bardouki et al., 2002; Hoffmann et al., 2016)
$MSIA (aq) + O_3 (aq) \rightarrow MSA (aq)$	3.50×10^7	(Hoffmann et al., 2016; Herrmann et al., 1998)
$MSI^- (aq) + O_3 (aq) \rightarrow MSA (aq)$	2.00×10^6	(Flyunt et al., 2001; Hoffmann et al., 2016)
$MSA (aq) + OH (aq) \rightarrow SO_4^{2-}$	1.50×10^7	(Hoffmann et al., 2016; Herrmann et al., 1998)
$MS^- (aq) + OH (aq) \rightarrow SO_4^{2-} (aq)$	1.29×10^7	(Zhu et al., 2003; Hoffmann et al., 2016)

246 **Table 3.** Overview of the DMS oxidation mechanism involving HPMTF formation.

Gas-phase reactions	Rate constant ($cm^3\ molecule^{-1}\ s^{-1}$)	References
$MSP (CH_3SCH_2OO) \rightarrow OOCH_2SCH_2OOH$	$2.2433 \times 10^{11} \exp(-9.8016e3/T) \times (1.0348 \times 10^8/T^3)$	(Berndt et al., 2019; Veres et al., 2020; Wollesen de Jonge et al., 2021)
$OOCH_2SCH_2OOH \rightarrow HPMTF$	$6.4970 \times 10^{11} \exp(-9.489e3/T) \times (1.1028 \times 10^8/T^3)$	(Berndt et al., 2019; Veres et al., 2020; Wollesen de Jonge et al., 2021)
$(HOOCH_2SCH_2OO) + OH \rightarrow OOCH_2SCH_2OOH + NO \rightarrow HOOCH_2S + NO_2 + HCHO$	$4.9 \times 10^{-12} \exp(260/T)$	MCMv3.3.1

Formatted
 Deleted: ([1]
 Formatted: Not Highlight
 Deleted: $0.60SO_2 + 0.4DMSO + CH_3O_2$
 Deleted: $8.2...5 \times 10^{-39} [O_2] e^{5376}$ [2]
 Deleted: $/(.../(1+1.05...5 \times 10^{-5}([$ [2]
 Deleted: (Burkholder et al., 2015; Pham et al., 1995; Spracklen et al., 2005)
 Formatted: Not Superscript/ Subscript
 Deleted: $]/[M]) e^{3644}$
 Deleted:) $cm^3\ molecule^{-1}\ s^{-1}$
 Formatted: Subscript
 Formatted: Not Superscript/ Subscript
 Deleted: $50e^{-14} \exp$
 Deleted: $50e$
 Deleted: (Burkholder et al., 2015; Du et al., 2007)
 Formatted: Not Superscript/ Subscript
 Deleted: 95MSIA + 0.05SO₂
 Deleted: $10e^{-12} \exp$
 Deleted: (Burkholder et al., 2015; von Glasow and Crutzen, 2004)
 Deleted: 9SO₂...5SO₂ + 0.1MSA
 Deleted: 00e
 Deleted: (Burkholder et al., 2015)
 Formatted: Not Superscript/ Subscript
 Deleted: O₃ → MSA
 Deleted: 2.00e-18
 Deleted: (von Glasow and Crutzen, 2004; Lucas and Prinn, 2002)
 Formatted: Not Superscript/ Subscript
 Deleted: (Sehested and Holzman, 1996; Hoffmann et al., 2016)
 Deleted: (Hoffmann et al., 2016)
 Deleted: (Hoffmann et al., 2016)
 Deleted: ([5]
 Deleted: O₃ → MSA
 Deleted: 2.00e-18
 Deleted: (von Glasow and Crutzen, 2004; Lucas and Prinn, 2002)
 Formatted: Not Superscript/ Subscript
 Deleted: ([6]
 Deleted: 2433e11*exp...433*10¹¹exp(-9.8016e3/T)*...*(1.0348e8...
 Deleted: 0970e11*exp...970*10¹¹exp(-9.489e3/T)*...*(1.1028e8...
 Deleted: 9e-12*exp
 Deleted: (Saunders et al., 2003)

MSP + HO ₂ → CH ₃ SCH ₂ OOH + O ₂	$1.13 \times 10^{-13} \exp(1300/T)$	MCMv3.3.1, (Wollesen de Jonge et al., 2021)
CH ₃ SCH ₂ OOH + OH → CH ₃ SCHO	7.03×10^{-11}	MCMv3.3.1
CH ₃ SCHO + OH → CH ₃ S + CO	1.11×10^{-11}	MCMv3.3.1
HPMTF + OH → HOOCH ₂ SCO + H ₂ O	4.00×10^{-12}	(Jernigan et al., 2022a)
HPMTF + OH → 0.13OCS + 0.87SO ₂ + CO	1.40×10^{-11}	(Jernigan et al., 2022a)
OCS + OH → SO ₂	$1.13 \times 10^{-13} \exp(1200/T)$	(Jernigan et al., 2022a)
HOOCH ₂ SCO → HOOCH ₂ S + CO	$9.2 \times 10^0 \exp(-505.4/T)$	(Wu et al., 2015)
HOOCH ₂ SCO → OH + HCHO + OCS	$1.6 \times 10^7 \exp(-1468.6/T)$	(Wu et al., 2015)
HOOCH ₂ S + O ₃ → HOOCH ₂ SO + O ₂	$1.15 \times 10^{-12} \exp(430/T)$	(Wu et al., 2015)
HOOCH ₂ S + NO ₂ → HOOCH ₂ SO + NO	$6.0 \times 10^{-11} \exp(240/T)$	(Wu et al., 2015)
HOOCH ₂ SO + O ₃ → SO ₂ + HCHO + OH + O ₂	4.0×10^{-13}	(Wu et al., 2015)
HOOCH ₂ SO + NO ₂ → SO ₂ + HCHO + OH + NO	1.2×10^{-11}	(Wu et al., 2015)

Table 4. Overview of the MSA-producing branch of the H-abstraction pathway of DMS oxidation.

Gas-phase reactions	Rate constant (cm ³ molecule ⁻¹ s ⁻¹)	References
DMS + OH → MSP (CH ₃ SCH ₂ OO) + H ₂ O	$1.12 \times 10^{-11} \exp(-250/T)$	JUPAC SOx22 (upd. 2006)
DMS + Cl → 0.45MSP + 0.55C ₂ H ₅ Cl + 0.45HCl	3.60×10^{-10}	(Fung et al., 2022; Enami et al., 2004)
C ₂ H ₆ SCl → DMSO + ClO	4.00×10^{-18}	(Hoffmann et al., 2016; Urbanski and Wine, 1999)
DMS + NO ₃ → MSP + HNO ₃	$1.9 \times 10^{-13} \exp(520/T)$	MCMv3.3.1, (Novak et al., 2021; Wollesen de Jonge et al., 2021; Atkinson et al., 2004)
MSP + NO → CH ₃ SCH ₂ (O) + NO ₂	$4.9 \times 10^{-12} \exp(260/T)$	MCMv3.3.1
MSP + MSP → 2HCHO + 2CH ₃ S	1.00×10^{-11}	(von Glasow and Crutzen, 2004)
CH ₃ SCH ₂ (O) → CH ₃ S + HCHO	1.0×10^6	MCMv3.3.1
CH ₃ S + O ₃ → CH ₃ S(O)	$1.15 \times 10^{-12} \exp(430/T)$	MCMv3.3.1; (Atkinson et al., 2004)
CH ₃ S + O ₂ → CH ₃ S(OO)	$1.20 \times 10^{-16} \exp(1580/T)$	MCMv3.3.1; (Atkinson et al., 2004)
CH ₃ S + NO ₂ → CH ₃ SO + NO	$3.00 \times 10^{-12} \exp(210/T)$	IUPAC SOx60 (upd. 2006); (Atkinson et al., 2004)
CH ₃ S(O) + O ₃ → CH ₃ (O ₂) + SO ₂	4.00×10^{-13}	JUPAC SOx61 (upd. 2006); (Borisenko et al., 2003)
CH ₃ SO + NO ₂ → 0.75CH ₃ SO ₂ + 0.75NO + 0.25SO ₂ + 0.25CH ₃ O ₂ + 0.25NO	1.20×10^{-11}	(Borisenko et al., 2003; Atkinson et al., 2004)
CH ₃ S(OO) → CH ₃ (O ₂) + SO ₂	$5.60 \times 10^{16} \exp(-10870/T)$	(Atkinson et al., 2004)
CH ₃ S(OO) → CH ₃ SO ₂	1.00	(Campolongo et al., 1999; Hoffmann et al., 2016)
CH ₃ S(OO) → CH ₃ S + O ₂	$3.50 \times 10^{10} \exp(-3560/T)$	MCMv3.3.1
CH ₃ SO ₂ + O ₃ → CH ₃ SO ₃ + O ₂	3.00×10^{-13}	MCMv3.3.1; (von Glasow and Crutzen, 2004)
CH ₃ SO ₂ → CH ₃ (O ₂) + SO ₂	$5.00 \times 10^{13} \exp(-9673/T)$	MCMv3.3.1; (Barone et al., 1995)

Deleted: 13e-...3*exp ... [8]
 Deleted: hv → CH₃SCH₂O +
 Deleted: J(41)
 Deleted: MCMv3.3.1, (Wollesen de Jonge et al., 2021)
 Deleted: 00e
 Formatted ... [9]
 Deleted: 40e
 Formatted ... [10]
 Deleted: 13e-...3*exp ... [11]
 Deleted: 2e9*exp
 Deleted: CH₂O
 Deleted: 6e7*exp
 Deleted: 15e-12*exp
 Deleted: (Saunders et al., 2003)
 Deleted: 0e-11*exp
 Deleted: (Saunders et al., 2003)
 Deleted: 0e
 Deleted: (Saunders et al., 2003)
 Formatted ... [12]
 Deleted: CH₂O
 Deleted: 2e
 Deleted: (Saunders et al., 2003)
 Formatted ... [13]
 Deleted: CH₂O
 Deleted: ()
 Deleted: Original
 Formatted ... [14]
 Deleted: 12e-11*exp
 Deleted: (Saunders et al., 2003)
 Deleted: 60e
 Formatted ... [15]
 Deleted: 00e
 Deleted: (Hoffmann et al., 2016)
 Formatted ... [16]
 Deleted: 9e-13*exp
 Deleted: (Novak et al., 2021; Wollesen de Jonge et al., 2021)
 Deleted: 9e-12*exp
 Deleted: (Saunders et al., 2003)
 Deleted: CH₃O₂ → CH₃SCH₂(O) + O₂
 Deleted: 3.74e-12
 Deleted: (Saunders et al., 2003)
 Formatted ... [18]
 Formatted ... [19]
 Deleted: CH₂O
 Deleted: 0e6
 Deleted: (Saunders et al., 2003)
 Deleted: + O₂
 Deleted: 15e-12*exp
 Deleted: (Saunders et al., 2003)
 Deleted: 20e-16*exp
 Deleted: (Saunders et al., 2003)
 Deleted: 00e
 Deleted: (Saunders et al., 2003)
 Formatted ... [20]
 Deleted: 60e16*exp
 Deleted: (Saunders et al., 2003)
 Deleted: (Saunders et al., 2003)
 Deleted: 00e
 Deleted: (Saunders et al., 2003)

$\text{CH}_3\text{SO}_2 + \text{NO}_2 \rightarrow \text{CH}_3\text{SO}_3 + \text{NO}$	2.20×10^{-11}	(Atkinson et al., 2004)
$\text{CH}_3\text{SO}_3 + \text{HO}_2 \rightarrow \text{MSA}$	5.00×10^{-11}	MCMv3.3.1; (von Glasow and Crutzen, 2004)
$\text{CH}_3\text{SO}_3 \rightarrow \text{CH}_3(\text{O}_2) + \text{H}_2\text{SO}_4$	$5.00 \times 10^{13} \exp(-9946/\text{T})$	MCMv3.3.1
$\text{MSA} + \text{OH} \rightarrow \text{CH}_3\text{SO}_3$	2.24×10^{-14}	MCMv3.3.1

429 To examine the sensitivities of size-resolved aerosol formation and growth to DMS chemistry
 430 modifications, model simulations are conducted as summarized in Table 5. Output from
 431 simulations MOD and MOD_noHetLossHPMTF was then compared against simulation BASE to
 432 understand the contribution of these additional chemical reactions on spatial pattern of the surface
 433 concentration of major oxidation products of DMS.

434 **Table 5.** List of mechanisms used in GEOS-Chem-TOMAS simulations.

Model Runs	Mechanism	HPMTF Cloud Loss*	HPMTF Aerosol Loss*
BASE	All reactions from Table 1	-	-
MOD_noHetLossHPMTF	All reactions from Table 2-4	Off	Off
MOD	All reactions from Table 2-4	On	On

435 * Instantaneous formation of sulfate via HPMTF cloud and aerosol loss uses a reactive uptake co-efficient (γ) of
 436 0.0016.

437 As shown in Table 2, the modified DMS chemistry simulations examined here include gas- and
 438 aqueous-phase oxidation of DMS and its intermediate oxidation products by OH, NO_3 , O_3 , and
 439 halogenated species as previously explored in an older version of GEOS-Chem (Chen et al., 2018).
 440 The aqueous-phase reactions in cloud droplets and aerosols were parameterized assuming a first-
 441 order loss of the gas-phase sulfur species (Chen et al., 2018). Further building upon this previous
 442 mechanism, the scheme used here also includes the formation and loss of HPMTF as previously
 443 tested in the global climate model CAM6-Chem as shown in Table 3 (Veres et al., 2020). Table 4
 444 presents the third piece of the mechanism: a gas-phase MSA-producing branch of the H-abstraction
 445 pathway in the DMS chemistry bridging the other two sets of the reactions (Fung et al., 2022). To
 446 avoid addition of SO_3 oxidation chemistry we have replaced SO_3 with H_2SO_4 followed by previous
 447 work for the decomposition reaction of CH_3SO_3 (Table 4). A similarly integrated mechanism
 448 (Table 2-4) has been previously explored using the CAM6-Chem model with a focus on radiation
 449 budget impacts, which is improved in this work through updates rate constants and the inclusion
 450 of additional relevant reactions (Fung et al., 2022; Novak et al., 2021; Wollesen de Jonge et al.,
 451 2021; Cala et al., 2023). The newly added reactions and their respective rate constants are largely
 452 based on the MCMv3.3.1 and the literature cited in the Table 2-4 reference list. We use a rate
 453 constant of $1.40 \times 10^{-11} \text{ cm}^3 \text{ molecules}^{-1} \text{ s}^{-1}$ for HPMTF + OH, which was previously determined
 454 based concentrations of other known sulfur species (DMS, DMSO, SO_2 and methyl thioformate;
 455 MTF; CH_3SCHO ; a structurally similar proxy to HPMTF) and evaluated by box model (Jernigan
 456 et al., 2022a). An exploration of reaction rate uncertainty for the HPMTF+OH reaction (Table 3),
 457 including both high and low end limits of $5.5 \times 10^{-11} \text{ cm}^3 \text{ molecules}^{-1} \text{ s}^{-1}$ and $1.4 \times$
 458 $10^{-12} \text{ cm}^3 \text{ molecules}^{-1} \text{ s}^{-1}$ resulted in only minor impacts on the fate of HPMTF and ultimate sulfate
 459 formation in our simulations (Novak et al., 2021; Wu et al., 2015).

460 Model sensitivity simulations were also performed with (case “MOD”) and without HPMTF
 461 heterogeneous uptake to clouds and aerosols (case “MOD_noHetLossHPMTF”) to account for
 462 how much of the DMS-derived HPMTF eventually forms SO_2 in the presence of these additional
 463 loss processes (Table 5). Previous work shows that aerosol surface chemistry causes additional

- Deleted: + O_2
- Deleted: 00e
- Deleted: (Saunders et al., 2003)
- Formatted: Superscript
- Deleted: 00e13*exp
- Deleted: (Saunders et al., 2003)
- Formatted Table

Deleted: A similarly integrated mechanism (Table 2-4) has been previously explored using the CAM6-Chem model with a focus on radiation budget impacts, with the exception of the $\text{DMS} + \text{NO}_3 = \text{MSP} + \text{HNO}_3$ reaction (included in Table 4) considered in this work (Fung et al., 2022; Novak et al., 2021; Wollesen de Jonge et al., 2021).

475 decreases in HPMTF mixing ratios, primarily over land, and that the loss of HPMTF in clouds is
476 larger (36%) than losses from aerosols (15%) when using an uptake coefficient of $\gamma = 0.01$ for both
477 processes (Novak et al., 2021). In this work, based on recent laboratory measurements, we use a
478 smaller uptake coefficient ($\gamma = 0.0016$) for HPMTF loss to aerosols and clouds (Table 5) (Jernigan
479 et al., 2022b). We assume HPMTF directly produces sulfate in cloud and aerosol followed but
480 previous work even though there is uncertainty in the fate of HPMTF heterogeneous loss (Zhang
481 and Millero, 1993; Novak et al., 2021; Jernigan et al., 2022a). For the aqueous-phase reactions
482 listed in Table 2, including the oxidation of intermediates DMSO and MSIA in cloud droplets and
483 aerosols, a first-order loss of the gas-phase sulfur species was assumed following previously used
484 parameterizations and physical parameter values (Chen et al., 2018). Alongside the gas-phase and
485 aqueous-phase reactions relevant to the added DMS oxidation mechanism contributing to the
486 formation of SO_2 and sulfate, the default version of GC-TOMAS used here also includes in-cloud
487 oxidation of SO_2 by H_2O_2 , O_3 , and O_2 catalyzed by transition metals (Mn, Fe), as well as the loss
488 of dissolved SO_2 by HOBr and HOCl , all of which are passed to TOMAS to account for sulfate
489 production (Chen et al., 2017; Wang et al., 2021).

490 All simulations are conducted for the year 2018, which was chosen to match the model simulation
491 with the dates of the NASA Atmospheric Tomography flight campaign (ATom-4) offering
492 observational data for HPMTF, DMS and SO_2 . Rate coefficients for all gas-phase sulfur reactions
493 are obtained from the most recent JPL report and other references while sulfur product yields for
494 gas-phase reactions are obtained from various laboratory and modeling studies (Burkholder et al.,
495 2020; Lucas and Prinn, 2002; Hoffmann et al., 2016; Gershenson et al., 2001; Kowalcuk et al.,
496 2003; Zhou et al., 2019; Jernigan et al., 2022a). The simulations included sea salt debromination
497 except for some sensitivity tests described below (Zhu et al., 2019; Schmidt et al., 2016). In all our
498 simulations including MOD, DMS is advected and undergoes chemical loss and transport but does
499 not undergo dry or wet deposition. However, dry and wet deposition of oxidation products such as
500 DMSO, MSIA, MSA and HPMTF are included.

501 We note that previous work has explored the impact of MSA on aerosol growth, including
502 modifications within TOMAS to represent this process (Hodshire et al., 2019). We do not include
503 this process here. Future work is recommended to examine its importance in the context of the
504 chemistry updates presented here.

505

3 Result and discussion

506

3.1 Model-Observations Comparison

507

3.1.1 Surface DMS mixing ratio

508 We compared the modeled DMS mixing ratio averaged for each month with the observational data
 509 collected at Crete Island (35° N, 26° E) and Amsterdam Island (37° S, 77° E) (Kouvarakis and
 510 Mihalopoulos, 2002; Chen et al., 2018; Castebrunet et al., 2009). Comparing simulations BASE
 511 and MOD, we find a closer match with DMS observations for simulations using modified DMS
 512 chemistry for both observation data shown in Figure 2. Modeled DMS mixing ratios calculated
 513 using base chemistry show strong positive bias during the months of May and June for Crete
 514 Island. By comparison, during the same period the modeled DMS mixing ratios calculated with
 515 modified chemistry reduces the bias from 102% to 42%. Similarly, for Amsterdam Island major
 516 overpredictions are apparent for the BASE simulation compared to MOD for the months of May-
 517 August. One reaction that may play a role in this shift is DMS + BrO, which as indicated earlier is
 518 responsible for a faster overall chemical loss of DMS, in particular over the southern hemisphere
 519 high latitudes. Beside DMS chemistry, sea surface DMS concentration is also proven to affect the
 520 modeled DMS mixing ratio (Chen et al., 2018). But the aim of this study is to investigate the
 521 chemistry aspect of DMS oxidation, so we did not explore how change in DMS seawater
 522 climatology and thus their emission influence the surface DMS mixing ratio.

Deleted: 44

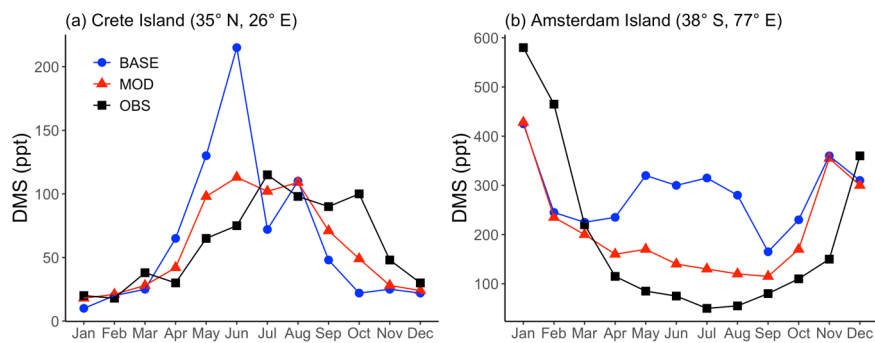


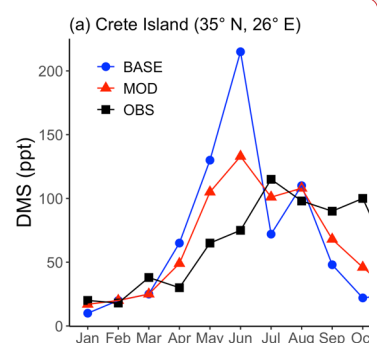
Figure 2 Observed (OBS) monthly mean surface DMS mixing ratios at (a) Crete Island and (b) Amsterdam Island compared with simulations BASE and MOD. Simulations are described in Table 5.

Deleted:

523

3.1.2 Comparison with aircraft observations

524 We further evaluate model output through a comparison with ATom-4 aircraft observations for
 525 specific days of measurement for DMS, HPMTF and SO₂ as shown in Figure 5. For this
 526 comparison, the model is sampled at the time and location of aircraft measurements by ATom-4
 527 using the planeflight diagnostic of GEOS-Chem.



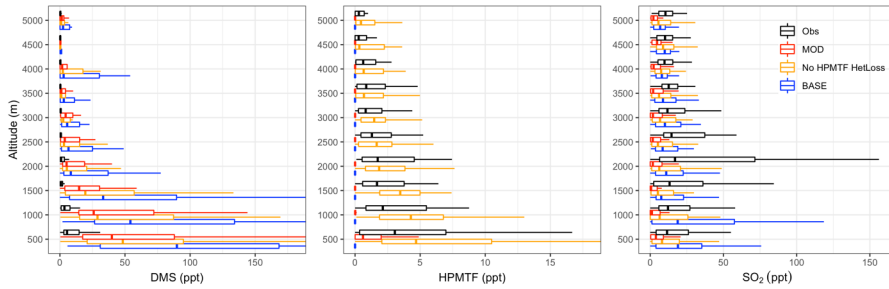
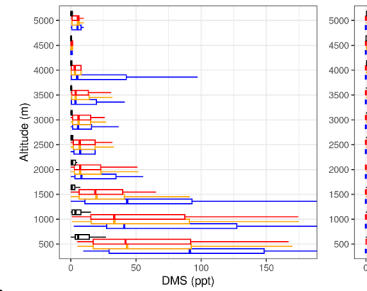


Figure 3 Vertical profiles of (a) DMS, (b) HPMTF and (c) SO₂ mixing ratios from ATom-4 observations (black) and model with simulation MOD sampled along the ATom-4 flight tracks (red) binned every 500 m of flight altitude. Also shown are modeled results without HPMTF heterogeneous loss with simulation MOD_{noHetLossHPMTF} (yellow), and for BASE GEOS-Chem chemistry (blue). Box plot whiskers show full range of distribution at each altitude bin. DMS observations are from Whole Air Samples (WAS) while HPMTF DC-8 observations are from iodide ion chemical ionization time-of-flight mass spectrometer (CIMS). SO₂ observations from ATom-4 campaign were measured by Laser Induced Fluorescence (LIF).

531 DMS concentrations measured during ATom-4 by whole air sampler (WAS) and modified
 532 chemistry simulation values for nearest neighbor grid cells are shown in Figure 3a across different
 533 altitudes. In general, the modeled DMS concentrations are significantly higher than those observed
 534 during ATom-4 missions especially close to the surface. However, model DMS concentrations
 535 decrease more rapidly than the measurement with altitudes indicating vertical mixing could be one
 536 of the underlying reasons for this trend. Even with this near surface bias, simulation MOD relative
 537 to BASE has greater DMS losses and a shorter DMS lifetime (from 1.5 d to 0.9 d) reducing the
 538 gap between modeled and observed concentration compared to simulation BASE. The reduction
 539 in modeled DMS is largest over the Southern Ocean (shown later in Fig. 5b) where oxidation by
 540 BrO and O₃ in the aqueous phase plays the major role in reducing DMS concentration, thereby
 541 reducing the model-observation bias (Fig. 3b). Remaining model biases could be at least partially
 542 attributed to model uncertainty in oxidant concentrations and cloud cover. The heterogeneous loss
 543 of HPMTF has minimal impact on DMS concentration and its vertical profile.

544 For HPMTF, Figure 3b shows that the observed and modeled HPMTF concentrations remain
 545 largely below 15 ppt. Agreement between observations and modeled HPMTF mixing ratios in the
 546 vertical profile (Fig. 3b) is poor for simulation MOD even close to the surface. Removing all
 547 heterogeneous loss of HPMTF improves model comparisons aloft, though surface concentrations
 548 become overestimated (yellow line of Fig. 3b), showing a high sensitivity to cloud and aerosol
 549 loss processes. We also find that the modeled HPMTF:DMS ratios range from 0.15:1 to 0.5:1 on
 550 a daily basis in most cases for when there is no heterogeneous loss of HPMTF, compared to 0.5:1
 551 observed during ATom-4 using the calibration maintained during measurement, implying
 552 reasonably good agreement for this value over daily time scales (Veres et al., 2020). The SARP
 553 flight campaign data has reported much lower HPMTF:DMS ratios (< 0.2) on cloudy days which
 554 is relatable to modeled HPMTF with simulation MOD (Novak et al., 2021). For simulation MOD,
 555 the modeled HPMTF:DMS ratio is 0.03:1 for until 0.5 km and then approaches zero with
 556 increasing altitude, indicating the need for additional work to better constrain production and loss
 557 processes of this intermediate. Our simulations indicate that cloud loss is the dominant modeled



Deleted:
 Formatted: Left

Deleted: 1

560 removal process of HPMTF, consistent with previous findings, while gas-phase OH oxidation
561 plays a minor role (Novak et al., 2021). Thus, the addition of cloud uptake dramatically decreases
562 HPMTF concentrations throughout the troposphere. Overall, this allows only ~~10%~~ of HPMTF
563 produced to end up as SO₂ with about ~~89%~~ lost to clouds and aerosol and thus removed from the
564 system, resulting net reduction in mean global SO₂ by about ~~40% along with other chemical~~
565 ~~processes involved for this reduction as well.~~ Previous work focusing entirely on gas-phase and
566 heterogeneous loss of HPMTF shows a much higher bias for both DMS and HPMTF during cloudy
567 and clear sky conditions using the same model and a condensed DMS oxidation mechanism,
568 indicating that the addition of gas-phase and heterogeneous oxidation of DMS including additional
569 intermediates such as DMSO and MSIA further reduce model biases for HPMTF with remaining
570 overestimation of the multiphase loss for HPMTF (Novak et al., 2021).

~~Deleted: 7~~

~~Deleted: 92~~

~~Deleted: 35%.~~

571 We also compared the SO₂ concentrations measured during ATom-4 by Laser Induced
572 Fluorescence (LIF) and simulation MOD values for nearest neighbor grid cells are shown in Figure
573 3c across different altitude. Modeled surface SO₂ concentrations are lower than those observed
574 during ATom-4 missions across the vertical scale shown here for simulation MOD. The greater
575 SO₂ losses results in a shorter SO₂ lifetime (from 1.4 d to 1.3 d) for simulation MOD relative to
576 simulation BASE. The reduction in modeled SO₂ is largest over the Southern Ocean (shown later
577 in Fig. 7a) where heterogeneous oxidation of HPMTF is most efficient and irreversible. Besides,
578 the OH addition channel of DMS does not directly produce SO₂ causing further reduction in the
579 concentration relative to BASE. Removing the heterogeneous loss of HPMTF increases the
580 modeled SO₂ compared to simulation MOD with underprediction remaining. Remaining model
581 biases could be at least partially attributed to uncertainty in DMS oxidation processes along with
582 other non-DMS sources contributing high concentration of SO₂. Aside from uncertainty in DMS
583 emissions and oxidation, recent understanding of marine sulfur chemistry such as methanethiol
584 (CH₃SH) oxidation has been reported as a significant source of SO₂ in the marine atmosphere
585 and could help reduce the bias, a possibility deserving further investigation (Berndt et al., 2023;
586 Novak et al., 2022). Overall the DMS oxidation chemistry implemented in this work reduces the
587 model observation bias close to the surface (up to 1km) compared to BASE GEOS-Chem
588 chemistry.

~~Deleted: for altitudes > 1km~~

589 Besides the vertical profile shown in Figure 3b, the global mean surface mixing ratio of HPMTF
590 with simulation MOD_noHetLossHPMTF for May 2018 is plotted in Figure 4 and compared with
591 the observational measurement of HPMTF made during the ATom-4 mission during the NASA
592 DC-8 flight campaign, which sampled the daytime remote marine atmosphere over the Pacific and
593 Atlantic Oceans. The ATom-4 measurements were carried out during daytime hours between April
594 24 and May 21, 2018 for 21 non-continuous days.

595 For this campaign, flight patterns covered vertical profiles from 0.2 to 14 km above the ocean
596 surface. The flight leg duration was 5 minutes and boundary layer altitude of 150 to 200 m above
597 the ocean surface. Since most of these measurement days are within the month of May 2018, here
598 we compare observations with modeled output of mean surface concentration of HPMTF for this
599 month. With the rate of isomerization reaction used in previous work, we find spatial patterns of
600 monthly mean surface concentrations are generally well captured (Jernigan et al., 2022a). Overall,
601 we find that the simulation MOD_noHetLossHPMTF results in better agreement with existing
602 overprediction for the vertical profile (Fig. 3b) and global surface layer HPMTF levels (Fig. 4)
603 compared to previous modeled approaches using the CAM-chem model (Veres et al., 2020).

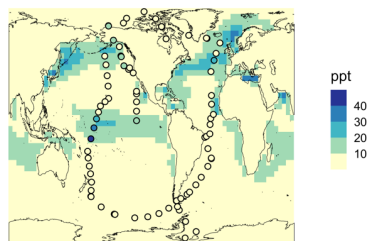
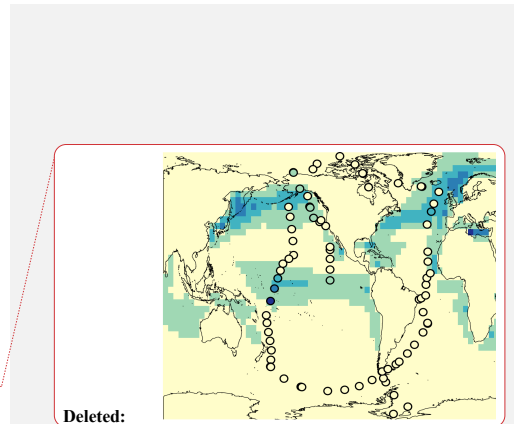


Figure 4 Geographic distribution of May 2018 monthly mean surface-layer mixing ratio of HPMTF for simulation MOD_noHetLossHPMTF mechanism represented for May 2018. The circles represent measurements of HPMTF during the ATom-4 mission by NASA DC-8 flight tracks with a limit of detection <1 ppt.

608
609

3.2 DMS burden and oxidation pathways

610 We find that the global burden of DMS in the MOD simulation is ~~65~~ Gg S (Table B1), ~~40%~~ lower
611 than what we find with the simulation BASE (108 Gg S). Even with this ~~42%~~ reduction, global
612 burdens are still well within the range of 9.6–150 Gg S suggested in other studies (Faloon, 2009;
613 Kloster et al., 2006). Figure 5a shows that surface DMS mixing ratios are highest in the North
614 Pacific and North Atlantic oceans for June-July-August (JJA) and in the Southern Ocean during
615 the months of December-January-February (DJF), revealing the underlying seasonality of DMS
616 emissions. According to previous studies, the highest DMS concentrations usually occur in
617 summer months due to higher rates of primary production in the presence of adequate solar
618 irradiation and high temperatures for both hemisphere (Galí et al., 2018; Lana et al., 2011; Wang
619 et al., 2020). In simulation MOD, the global mean surface-layer DMS burden was higher in SH
620 for DJF and lower in NH for JJA which is due to larger ocean area in the SH than NH. We also
621 find that the reactions of this expanded DMS oxidation mechanism collectively contribute to
622 reductions in mean surface-layer DMS concentration of ~~58%~~ and ~~22%~~ compared to BASE for JJA
623 and DJF respectively (Fig. 5b). These reductions are due primarily to the addition of multiple new
624 chemical loss pathways compared to BASE, which are especially impactful during JJA months
625 due to elevated BrO in the SH winter and also higher O₃ and OH concentration in the NH
626 summer compared to the SH summer (Zhang et al., 2018; Pound et al., 2020).



Deleted:

Deleted: 67

Deleted: 38

Deleted: 38

Deleted: 60

Deleted: 23

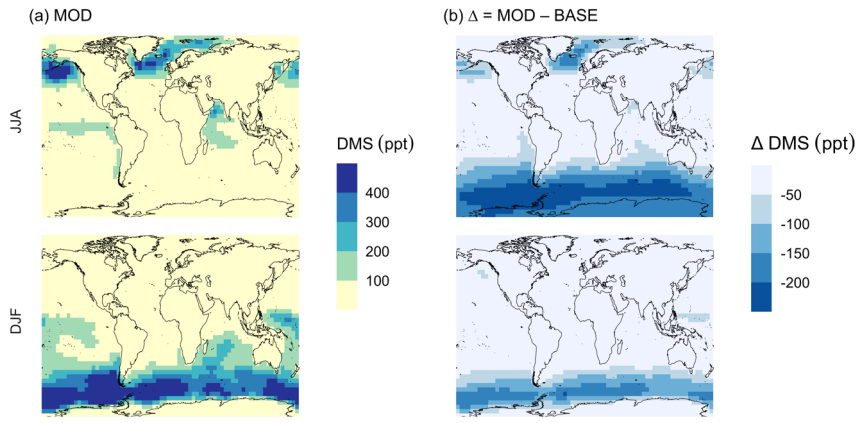
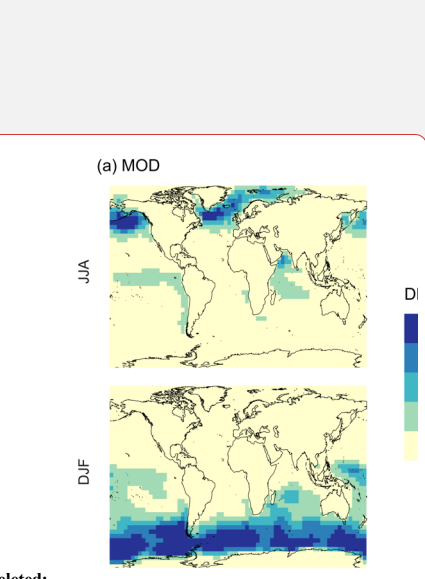


Figure 5 Geographic distribution of mean surface DMS mixing ratio (ppt) for simulation (a) MOD and (b) difference between simulations from its baseline, $\Delta = \text{MOD} - \text{BASE}$ from GEOS-Chem simulations. Here, JJA and DJF represent June-July-August and December-January-February respectively. Simulations are described in Table 5.

As shown in Fig. 5b, this DJF DMS reduction is seen mainly over the Southern Ocean and is largely attributable to faster chemical losses through the added reactions of $\text{DMS} + \text{BrO}$ and $\text{DMS}_{(\text{aq})} + \text{O}_3_{(\text{aq})}$, which in earlier work was hypothesized as a possible reason for high model biases in the absence of detailed halogen chemistry (Chen et al., 2016). The global lifetime of DMS decreases from 1.5 days in the BASE simulation to 0.9 day in the MOD simulation.

These values are comparable to the range of 0.8–2.1 d reported by previous studies (Chen et al., 2018; Fung et al., 2022). The global DMS emission flux (F_{DMS}) from ocean to the atmosphere is 22 Tg S yr⁻¹ and is within the range of 11– 28 Tg S yr⁻¹ simulated by GEOS-Chem and other models in previous studies (Lennartz et al., 2015; Fung et al., 2022; Chen et al., 2018; Hezel et al., 2011; Spracklen et al., 2005). Our F_{DMS} is higher than the 18 Tg S yr⁻¹ which uses sea surface DMS concentration from Kettle et al. (1999) as reported (Chen et al., 2018) indicating the DMS emission varies with change in sea surface DMS climatology. The analysis and improvement of DMS emissions directly is not a part of this work, but we note that improved and validated inventories for DMS will certainly play a role in subsequent oxidation product comparisons. We recommend ongoing evaluation of DMS emissions inputs to complement the expanded chemical mechanism development we present here.

In the BASE simulation the chemical loss of DMS acts as its only sink (as opposed to dry and wet deposition), leading to a full conversion yield of DMS into SO_2 (82.5%) and MSA (17.5%) (Fig. A3a). Figure 6 shows that in simulation MOD with updated DMS oxidation scheme DMS is mainly oxidized by OH in the gas phase, with 27.6% of losses proceeding via the H-abstraction channel and 38.6% via the OH-addition pathway, together contributing up to 66.2% of global average loss with high regional contribution over the tropical oceans via the abstraction channel where surface OH is the highest. NO_3 oxidation of DMS accounts for another 11.2% of global DMS chemical losses, comparable to values found in previous studies (Chen et al., 2018; Fung et



Deleted: 1.

Deleted: 1.

Deleted: 33.5

Deleted: 29.4

Deleted: 62

Deleted: 12.8

663 al., 2022). Over the ocean, the NO_3 loss pathway is strongest in the NH coastal regions due to
664 outflow of NO_x sources from over the land whereas for the SH values are generally less than 10%.
665 Oxidation by BrO is responsible for 18.4% of the global DMS removal, falling within the
666 previously estimated range of 8%–29% (Boucher et al., 2003; Khan et al., 2016; Chen et al., 2018).
667 Regionally, its contribution can reach 50%–60% over high latitudes of the Southern Hemisphere
668 as well as to the north near the Arctic Ocean, consistent with previous box model studies based on
669 the availability of high BrO and low OH and NO_3 for those regions (Hoffmann et al., 2016). DMS
670 + O_3 accounts for 2.2% (aqueous) and 0.9% (gas phase) of global surface DMS loss. The higher
671 contribution from BrO and lower from O_3 using this mechanism compared to some previous
672 studies could be explained in part by the recently implemented sea-salt debromination mechanism
673 in GEOS-Chem, resulting in a much higher background level of BrO as well as lower O_3
674 abundance, especially in the southern hemisphere (Boucher et al., 2003; Chen et al., 2018; Fung
675 et al., 2022; Sherwen et al., 2016a; Wang et al., 2021). To further quantify the importance of the
676 sea salt debromination mechanism, we perform an emissions sensitivity test by turning this
677 emission source off while using updated MOD chemistry (Fig. A1). As would be expected, these
678 simulations show much lower BrO formation (as shown in Fig. A6) and resulting chemical
679 impacts, with overall oxidation contributions comparable to previous literature (Schmidt et al.,
680 2016; Wang et al., 2021). We find that under this scenario the relative contribution of BrO for
681 DMS loss decreases to 2.2%, while the DMS + O_3 pathway increases to 43.3% (aqueous) and 1.4%
682 (gas phase), and the DMS + OH pathway increases to 31.0% (abstraction) and 48.0% (addition)
683 of global surface DMS loss (Fig. A1). The DMS loss via interaction with NO_3 also increases to
684 2.0% when sea salt debromination is turned off in the mechanism. The relative contributions of
685 other oxidants remain mostly unaffected in the BrO sensitivity test.

Deleted: 19.6

Deleted: 7

Deleted: 1.1

Deleted: 3.8

Deleted: 4.0

Deleted: 8

Deleted: 38

Deleted: 36.1

Deleted: by

Deleted: 5

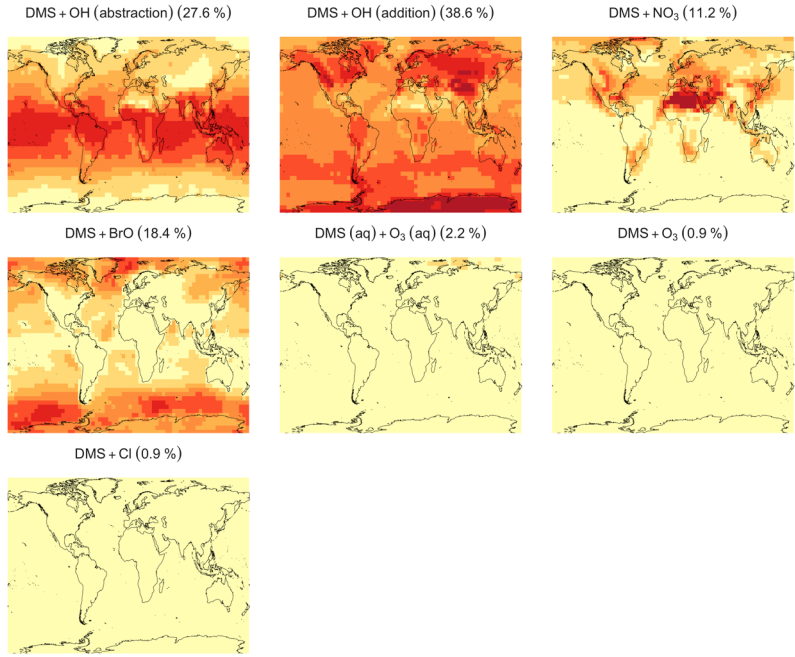
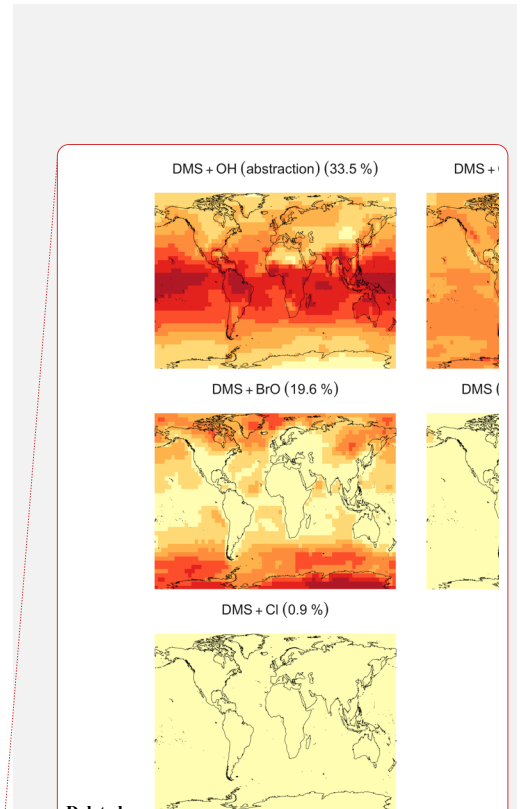


Figure 6 Geographic distribution of the annual mean surface layer fraction of total DMS oxidation (percent) attributed to different tropospheric oxidants for simulation MOD (described in Table 5). Percentages in parentheses indicate the average contribution to global chemical loss for the fraction of DMS emitted for each reaction pathways presented here.



Deleted:

Deleted: indicates

Deleted: ,

Deleted: and 1.0% respectively

696 Regionally, the fractional contribution of aqueous-phase DMS + O₃ to DMS oxidation can be up
 697 to 10%–20% over high-latitude oceans, especially with the sea salt debromination is turned off
 698 (Fig. A1), which is in the middle of the 5%–30% contribution to high-latitude DMS losses
 699 previously reported (Chen et al., 2018; Fung et al., 2022; von Glasow and Crutzen, 2004). The Cl
 700 oxidation reaction contribute about 0.9% for with and without sea salt debromination to the
 701 chemical removal of DMS, consistent with some previous studies (Atkinson et al., 2004; Fung et
 702 al., 2022). This does differ from other reported values however, including those from a global
 703 model study (4%) and box model simulations (8%–18%) (Chen et al., 2018; Hoffmann et al.,
 704 2016; von Glasow and Crutzen, 2004). It's worth noting that none of the studies reporting such
 705 high Cl contributions included HPMTF formation and loss. Ongoing uncertainties associated with
 706 model-observation bias of Cl should be further resolved to get better representation of halogenated
 707 species contributions to DMS loss (Wang et al., 2021). Due to slower reaction kinetics and lower
 708 fractional contribution reported earlier compared to BrO with DMS and uncertainty in surface
 709 concentration and kinetics for photochemically generated halogenated species such as Br, IO we
 710 did not include them in our chemical scheme (Chen et al., 2018).

711 3.3 Implications of the extended DMS oxidation mechanism

716 Figure 7 shows that the MOD simulation results in ~~40%~~ reduction of surface layer SO_2 relative to
 717 BASE, but a huge increase in SO_4^{2-} in most regions. These changes suggest that the combination
 718 of gas-phase and aqueous-phase reactions results in a higher net yield of MSA and HPMTF and a
 719 lower net yield of gas-phase SO_2 . Additionally, comparison of simulation MOD relative to
 720 MOD_noHetLossHPMTF (Fig. A2a) shows that loss of HPMTF in cloud droplets and aerosol
 721 reduces the global mean production of SO_2 by ~~21.4%~~, contributing to the SO_2 reduction and
 722 increasing mean surface layer sulfate by ~~12.4%~~ (Fig. A2b). This reduction in SO_2 is expected to
 723 reduce the availability of gas-phase sulfuric acid for new particle formation by nucleation (Clarke
 724 et al., 1998a). Total SO_4^{2-} increases over the ocean, however, because the increased SO_4^{2-}
 725 production from rapid loss of MSA and HPMTF in aqueous-phase offsets the reduced oxidation
 726 of SO_2 (Fig. 7b). ~~In addition to that, reduced gas-phase sulfur species such as CH_3SO_3 also
 727 contribute to sulfate formation in our mechanism as followed by other works (Fung et al., 2022).~~

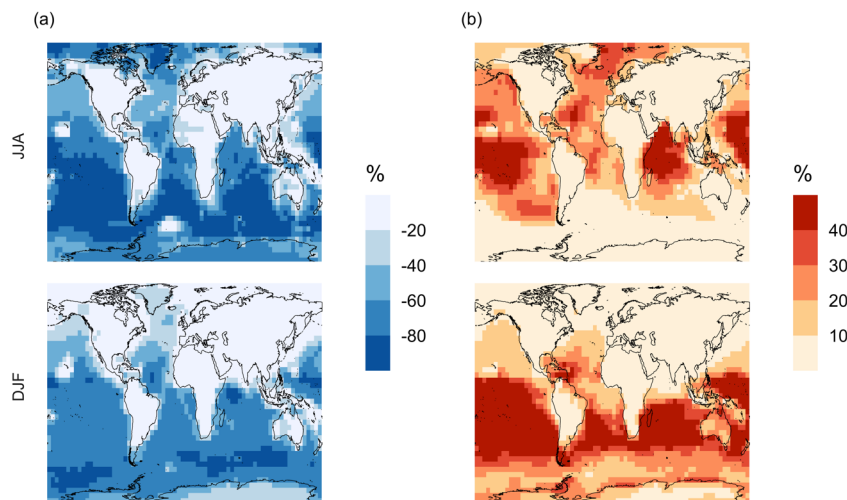


Figure 7 Percent change in simulated surface layer (a) SO_2 and (b) SO_4^{2-} for simulation MOD relative to BASE for June, July and August mean (JJA) and December, January, and February mean (DJF). Simulations are described in Table 5.

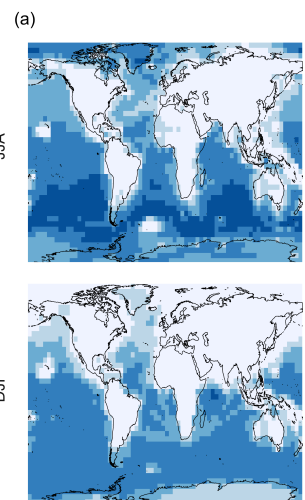
729 Qualitatively, the regions showing the highest percent changes of SO_2 are consistent with previous
 730 studies that included HPMTF chemistry and loss processes though the extent of this reduction is
 731 much higher with the integrated mechanism used in our study (Fig. 7a) (Novak et al., 2021). The
 732 regions with the largest percent change in SO_2 reduction are those where DMS oxidation
 733 contributes most to SO_2 , and where HPMTF production and in-cloud oxidation of HPMTF are
 734 efficient. This spatial pattern thus helps us to identify where the production and heterogeneous loss
 735 of HPMTF and MSA is enhanced. One of the reactions that possibly contributes to delayed
 736 formation and reduction of SO_2 concentration is the first-generation OCS formation from OH
 737 oxidation of HPMTF. We find that addition of cloud and aerosol loss significantly decreases the
 738 OCS production, especially in high cloud cover regions as previously reported (Jernigan et al.,

Deleted: 35

Deleted: 19.6

Deleted: 16.1

Deleted:



743 2022a). Even though the cloud loss of HPMTF increases the production of surface sulfate, the total
 744 global sulfate burden we calculate increases by only ~~6.5%~~ from the BASE sulfate burden of around
 745 575 Gg S. This can be attributed to minor contribution of DMS and its intermediate oxidation
 746 products in SO_2 production compared to other non-DMS derived sources. In addition, the
 747 production of stable intermediate oxidation products delay the conversion of SO_2 to SO_4^{2-} and
 748 modify its spatial distribution in the marine environment. Thus, we should expect these aqueous
 749 phase oxidation products to contribute to particle mass rather than increase the number of nucleated
 750 particles, as suggested in other studies (Clarke et al., 1998b; Novak et al., 2021; Williamson et al.,
 751 2019).

752

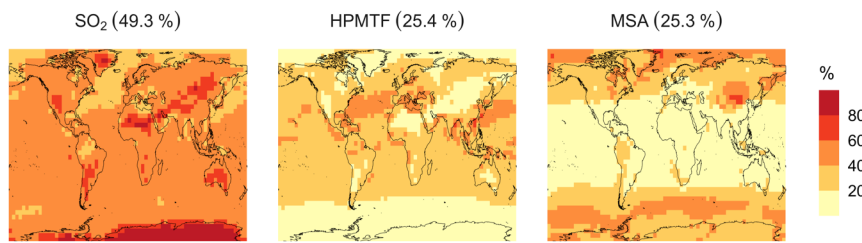


Figure 8 Simulated branching ratio (in %) of the DMS oxidation mechanism considering SO_2 , HPMTF and MSA as major terminal oxidation products calculated from their annual total production rate for simulation MOD.

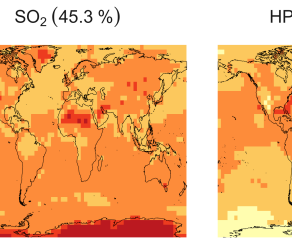
753 The spatial distribution of product branching ratios of DMS oxidation is shown in Figure 8. Here,
 754 ~~25.4%~~ of the annual total DMS oxidation will end up as HPMTF, while final SO_2 yield decreases
 755 to ~~49.3%~~ compared to 82.5% for the BASE simulation (Fig. A3a). The terminal HPMTF branch
 756 represents sulfur removed from the system by cloud and aerosol uptake of HPMTF, leading to a
 757 reduced overall formation of SO_2 . With sea salt debromination turned off, modified chemistry
 758 forms even more HPMTF (~~27.7%~~), slightly higher SO_2 (~~51.3%~~), and lowers the yield of MSA to
 759 ~~21.0%~~ (~~25.3%~~ with the sea salt debromination on), underscoring the importance of halogen
 760 chemistry for MSA production (Fig. A3b). These results are comparable with observationally
 761 constrained estimates from ATom-4 flight campaigns, where $\sim 30\% - 40\%$ DMS was oxidized to
 762 HPMTF along their flight tracks compared to ~~27.7%~~ for the full branch of HPMTF in the present
 763 work, as well as with previous modeling studies showing 33% HPMTF formation as terminating
 764 product (Veres et al., 2020; Fung et al., 2022). MSA is produced mostly by aqueous phase
 765 oxidation of MSIA by O_3 and OH according to the mechanism used here and has high abundance
 766 near the Southern Ocean and Antarctic belt as reported by previous studies (Chen et al., 2018;
 767 Hoffmann et al., 2016; Fung et al., 2022). The global burden of MSA decreases dramatically, from
 768 19 Gg S for 'Base' to ~~9.2~~ Gg S for simulation MOD. The higher rate of major loss process or lower
 769 rate of production of MSA from the aqueous phase reactions could be responsible for this reduction
 770 in global budget (Fung et al., 2022).

771 3.4 Impact on aerosol size distributions

772 Following the percent change in simulated surface layer SO_2 and SO_4^{2-} for modified DMS
 773 chemistry (Fig. 7), we further explore how this expanded DMS oxidation chemistry impacts
 774 modeled aerosol size distributions. Figure 9 shows the global mean surface-layer percent change
 775 in the normalized aerosol number concentration for modified chemistry relative to the BASE

Deleted: 4.1

Deleted:



Deleted: 34

Deleted: 45

Deleted: 41

Deleted: 46.4

Deleted: 11.9% (19)

Deleted: broadly consistent

Deleted: 34.4

Deleted: 8.5

786 simulation, with and without cloud and aerosol HPMTF loss processes. The aerosol number
 787 concentration decreases for the sub-80 nm diameter size bins for both simulations, especially
 788 during the DJF months when cloud and aerosol loss pathways of HPMTF are included (MOD
 789 case), demonstrating the negative impact of these processes on simulated new particle formation.
 790 Without these processes included (as in case MOD_noHetLossHPMTF), percent changes are
 791 **lower relative to simulation MOD but similar in terms of direction of changes.** On the other hand,
 792 HPMTF lost to clouds and aerosols increases the simulated number of particles with diameter
 793 above 100 nm in the MOD simulation, consistent with the increase in sulfate mass concentrations
 794 shown in Fig. 7 and suggesting that HPMTF heterogenous loss promotes simulated particle growth
 795 to diameters larger than 80-100 nm. The greater abundance of particles larger than 100 nm also
 796 acts as a condensation sink, further suppressing nucleation and growth at smaller size ranges.

Deleted: far more modest for these smaller size ranges.

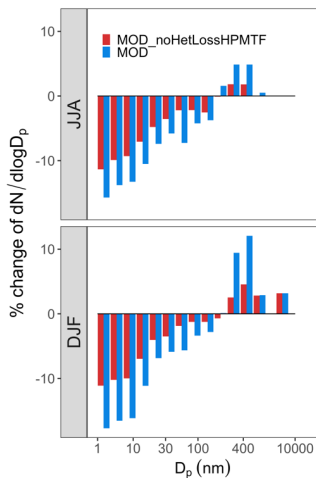


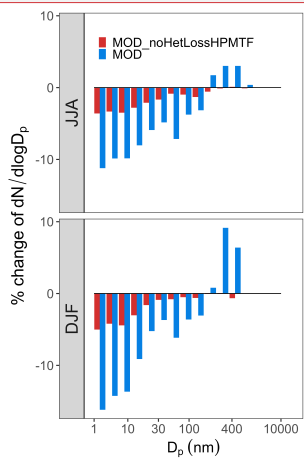
Figure 9 Global mean surface-layer percent change in normalized aerosol number concentration for different size bins with particle diameter, D_p in the range of $3 \text{ nm} < D_p < 10000 \text{ nm}$ for simulations MOD and MOD_noHetLossHPMTF relative to simulation BASE. Simulations are described in Table 5.

797 The geographic distribution of surface layer aerosol number concentration for aerosol in the size
 798 range of 3 – 80 nm for two seasons is shown in Figure 10. We find that global mean aerosol number
 799 concentration in this size range decreases for simulations MOD and MOD_noHetLossHPMTF
 800 relative to BASE by **16.8%** and **11.7%** respectively. Decreases are greater for simulation MOD
 801 (Fig. 10b). Fig. 10c shows the effect of HPMTF heterogenous loss processes on the number of
 802 particles with diameters between 3-80 nm for simulation MOD relative to simulation
 803 MOD_noHetLossHPMTF. The largely negative impact of HPMTF loss to clouds and aerosols on
 804 sub-80 nm particle number is contributed to by enhanced direct sulfate formation on pre-existing
 805 particles, bypassing gas-phase SO_2 formation (a precursor for new particle formation). As well, in
 806 the model, new particles grow through condensation of H_2SO_4 and organics and their growth are
 807 dependent on the condensation sink, while loss of particle number depends on the coagulation
 808 sink. Thus, changes to the condensation/coagulation sinks and sulfuric acid production rate
 809 through the updated mechanism will also alter the growth rates of small particles (sub-80 nm) as

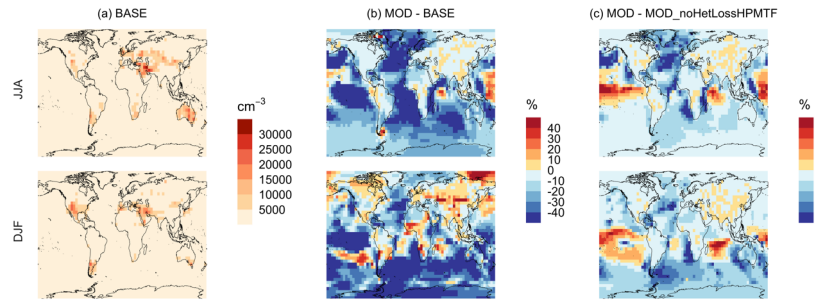
Deleted:

Deleted: 12

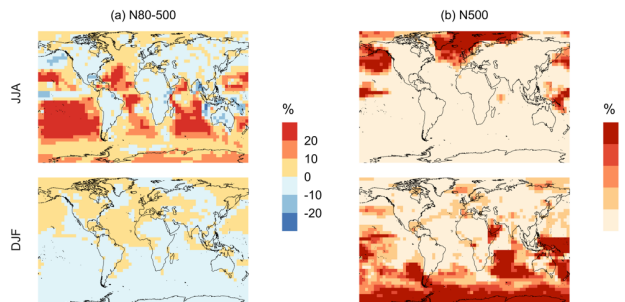
Deleted: 9.9



814 well as their coagulation loss rates. Hence, similar to the discussion for Figure 9, the reduction of
 815 gas-phase production of H_2SO_4 in MOD relative to BASE slows new-particle formation and
 816 growth, while the additional production of sulfate through aqueous chemistry on larger particles
 817 in MOD increases the coagulation scavenging of the newly formed particles. These two effects
 818 synergistically reduce the concentration of ultrafine particles in the model. The fraction of newly
 819 formed particles that can reach the CCN size is dependent on the particle growth rates, especially
 820 for particle sizes below 10 nm, where we see highest coagulation losses to larger particles. The
 821 sensitivity of these results to the new sea salt debromination parameterization is shown in Fig. A4,
 822 where we find a regional increase in aerosol number concentration at mid to higher latitude of the
 823 SH despite low BrO concentrations (Fig A4).

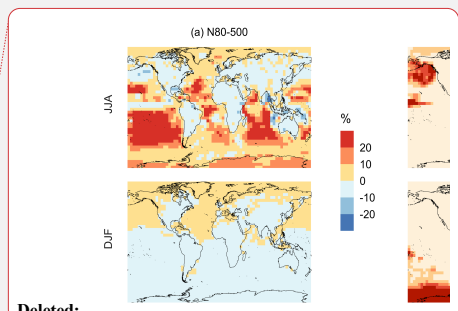
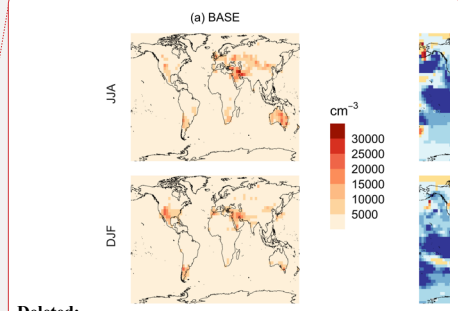


824 **Figure 10** Geographic distribution of seasonal-mean surface-layer aerosol number concentration in cm^{-3} (for
 825 particles with diameters between 3 – 80 nm) for (a) the BASE simulation, (b) the percent difference between
 826 MOD and BASE and (c) the percent difference between MOD and MOD_noHetLossHPMTF to show the role
 827 of cloud and aerosol loss of HPMTF. The top and the bottom rows correspond to the months of JJA and DJF
respectively. Simulations are described in Table 5.



828 **Figure 11** Geographic distribution of percent difference in seasonal-mean surface-layer aerosol number
 829 concentration in cm^{-3} for simulations MOD relative to simulations BASE for diameters between (a) 80 – 500 nm
 830 and (b) >500 nm. Simulations are described in Table 5.

831 Finally, we also analyze the impact of this expanded DMS scheme on particles larger than 80 nm
 832 (Fig. 11). We find increases of around 6.7% for JJA mean surface layer number concentration of
 833 aerosol with diameters between 80-500 nm, while DJF months show mean reductions of -5.4% for



Deleted: 6

831 DJF despite largely positive changes in the marine NH for these months (Fig. 11a). However, for
832 the > 500 nm size ranges (Fig. 11b), the global mean surface layer number concentration of aerosol
833 mostly increases, with highest changes occurring in the areas of peak DMS emission in both
834 hemispheres, during their summertime season. A similar trend is observed in the absence of cloud
835 and aerosol HPMTF uptake in simulation MOD_noHetLossHPMTF (Fig. A5). Overall, the global
836 annual mean number of particles with diameter larger than 80 nm increases by about 3.8%.

837 Comparing the regional extent and direction of change in particle number concentration, we find
838 the net increase in particle number concentration is higher for MOD compared to
839 MOD_noHetLossHPMTF, highlighting the importance of HPMTF loss processes to clouds and
840 aerosols as a contributor of CCN.

841

Deleted: this

843 **4 Conclusion**

844 In this study we update the default DMS oxidation scheme in the GEOS-Chem model by
845 implementing an integrated oxidation mechanism. The new scheme includes gas-phase and
846 aqueous phase reactions involving DMSO, MSIA and HPMTF formation, as well as newly
847 identified HPMTF loss processes yielding considerable changes in seasonal concentrations of
848 major oxidation products and sulfur-derived aerosols. With this new chemistry scheme, global
849 annual mean surface DMS concentration decreases by ~~36%~~ relative to the BASE scheme in GEOS-
850 Chem globally due to the presence of additional loss processes in the integrated mechanism
851 reducing the bias to ATom-4 DMS measurement.

Deleted: 38

852 In this new scheme, OH, BrO, O₃ and NO_x species act as important sinks of DMS contributing to
853 ~~66.2%, 18.4%, 3.1% and 11.2%~~ global annual mean surface DMS loss, highlighting the relative
854 importance of these loss process in determining surface DMS budget. We also find that at higher
855 latitudes, gas phase and multiphase oxidation of DMS by O₃ and BrO becomes important to
856 determine the budget of DMS. On the other hand, overall OH is responsible for major loss of DMS
857 via the addition and abstraction reaction relative to other sinks with more contribution from the
858 addition reaction compared to abstraction reaction. For the global distribution of simulated
859 HPMTF, our updated scheme in GEOS-Chem provides a reduced high bias against observations
860 compared to previous studies. While emissions of BrO are uncertain in this version of GEOS-
861 Chem, we find that the compound acts as a key sink of DMS, especially over the Southern Ocean.
862 Overall, we find large reduction in SO₂ (~~40%~~) and an increase in sulfate (~~17%~~) due to the addition
863 of heterogeneous HPMTF loss processes.

Deleted: 62.9%, 19.6

Deleted: 8

Deleted: 12.8

Deleted: at lower latitudes

Deleted: contribute to a greater extent

Deleted: other sinks and at comparable extent to previous
Deleted: studies exploring this chemistry

Deleted: 35

Deleted: 22

Deleted: 12

Deleted: 1

Deleted: 6

864 The lower SO₂ with the new DMS chemistry scheme contributes to a reduction in the global annual
865 mean surface layer number concentration of particles with diameters less than 80 nm by ~~16.8%~~,
866 contributed to by reductions in gas-phase precursors for new particle formation. There is a
867 concurrent increase of ~~3.8%~~ in the global annual mean number of particles with diameters larger
868 than 80 nm. This latter global mean particle number change varies in sign seasonally, with a ~~6.7%~~
869 increase for JJA, and a 5.4% decrease for DJF. This decrease is dominated by southern hemisphere
870 summertime changes, connected with suppressed new particle formation/growth and enhanced
871 coagulation following additional sulfate production through aqueous chemistry. Cloud loss
872 processes related to HPMTF make key contributions to these simulated changes through
873 enhancement of aqueous-phase particle growth of those particle large enough to act as CCN.

Deleted: 35

Deleted: 22

Deleted: 12

Deleted: 1

Deleted: 6

874 Although the increased chemical mechanism complexity described in this work will necessarily
875 increase model computational cost (MOD simulation run times increase by approximately 16%),
876 this study highlights the value of including a more realistic chemical oxidation mechanism of DMS
877 and its stable intermediates for better representation of DMS-derived aerosol in the marine
878 atmosphere, as well as its seasonal size distributions. A reduced form of the key chemical species
879 and pathways should be able to capture the key processes with less computational impact and will
880 be a priority in future work.

894 **Appendix A: Additional figures**

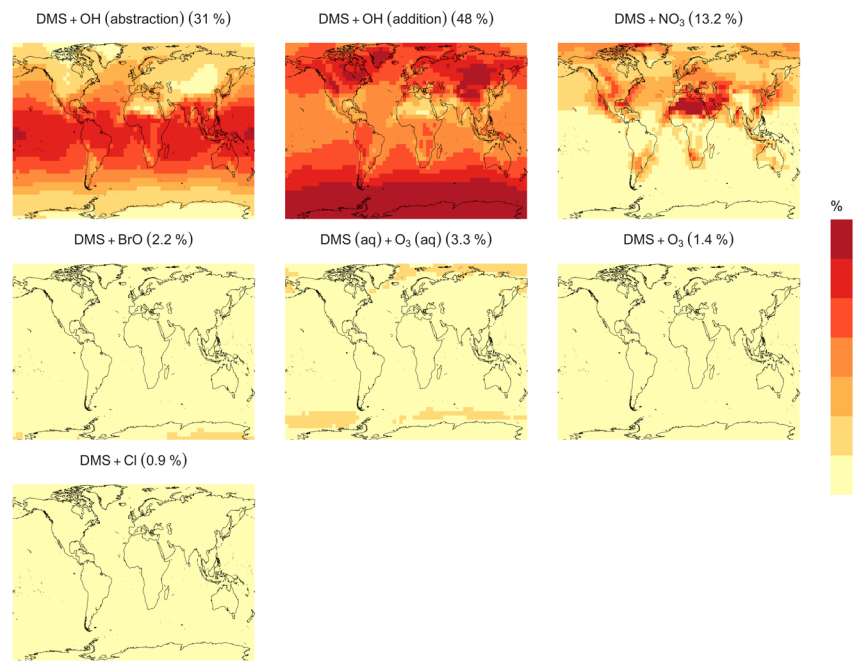
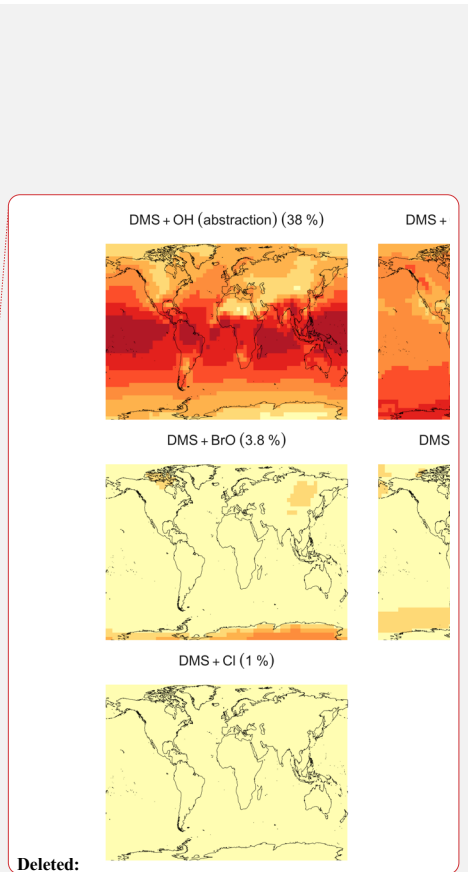


Figure A1 Surface layer geographic distribution of the simulated annual mean fraction of total DMS oxidation (percent) attributed to different tropospheric oxidants for a simulation otherwise the same as simulation MOD except with no sea salt debromination. Percentages in parentheses indicates average contribution to global chemical loss as a fraction of DMS emitted for each reaction pathways presented here. Simulations are described in Table 5.

895



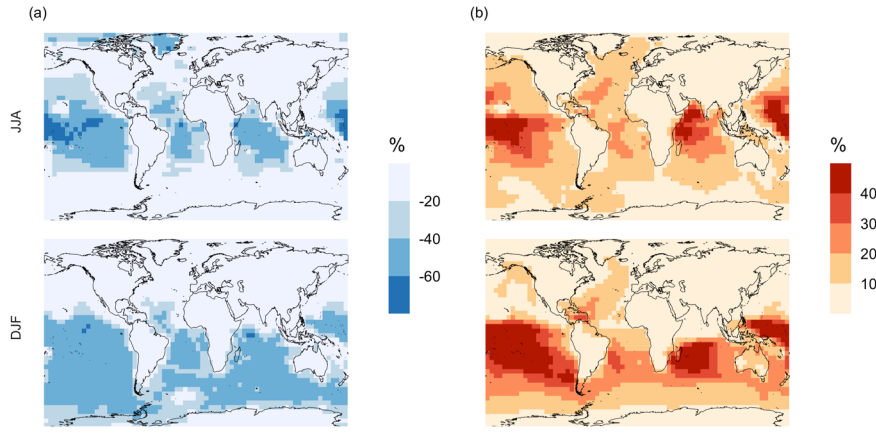


Figure A2 Percent change in simulated surface layer (a) SO_2 and (b) SO_4^{2-} for simulation MOD relative to MOD_noHetLossHPMTF for June, July and August mean (JJA) and December, January, and February mean (DJF). Simulations are described in Table 5.

897

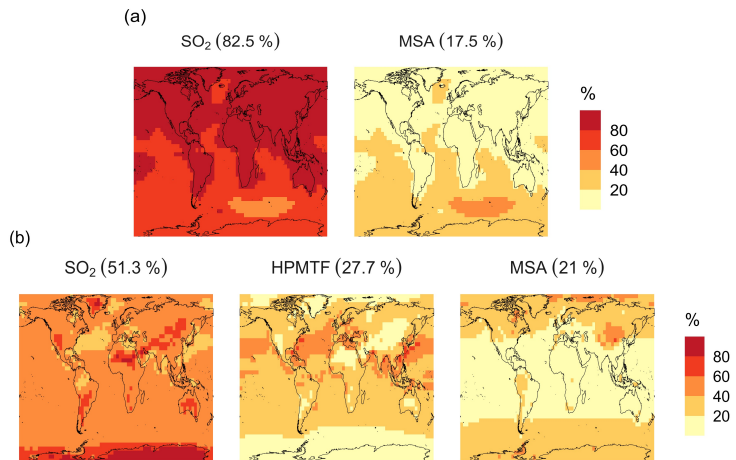
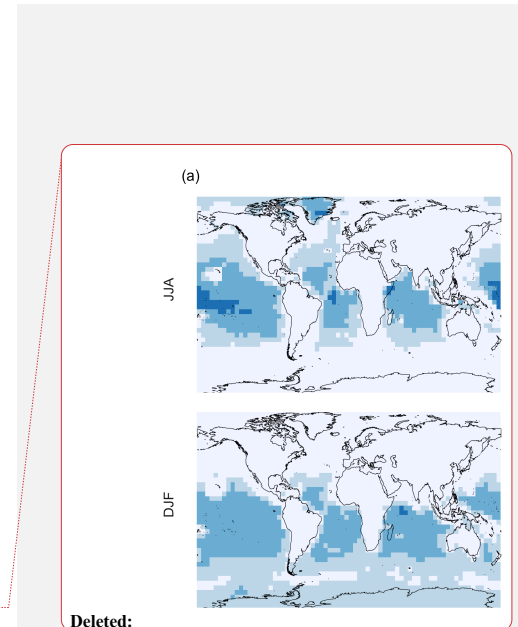
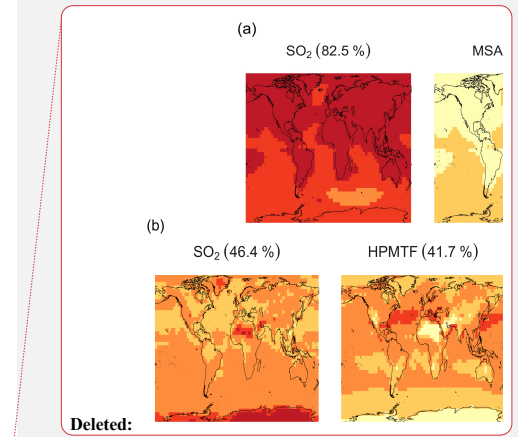


Figure A3 Simulated annual mean surface layer branching ratios (in %) of the DMS oxidation mechanism considering SO_2 , HPMTF, and MSA as major oxidation products calculated from their total production rates for simulations similar to (a, top row) BASE and (b, bottom row) MOD, except MOD with no sea salt debromination. Simulations are described in Table 5.

898



Deleted:



Deleted:
Deleted:
Deleted:

Formatted Table

Deleted: all

Deleted:

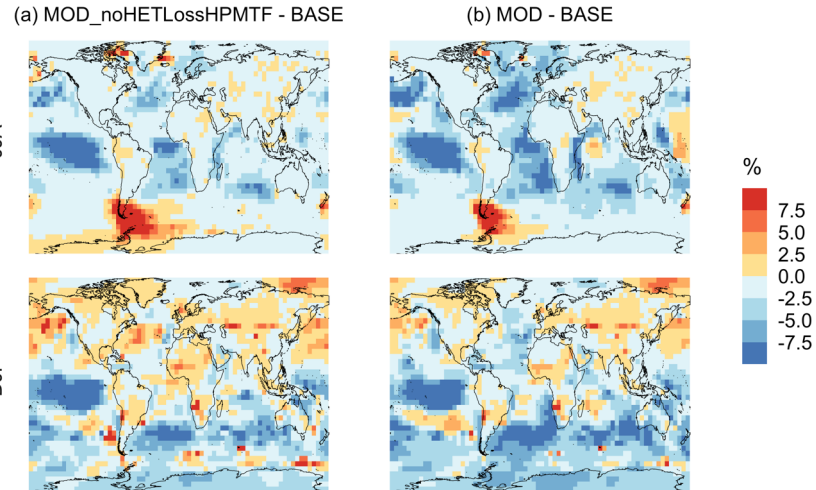


Figure A4 Geographic distribution of percent difference in seasonal-mean surface-layer aerosol number concentration in cm^{-3} (for particles with diameters between 3 – 80 nm) for simulations similar to (a) MOD_noHETLossHPMTF and (b) MOD relative to simulations BASE, except all with no sea salt debromination. Simulations are described in Table 5.

903

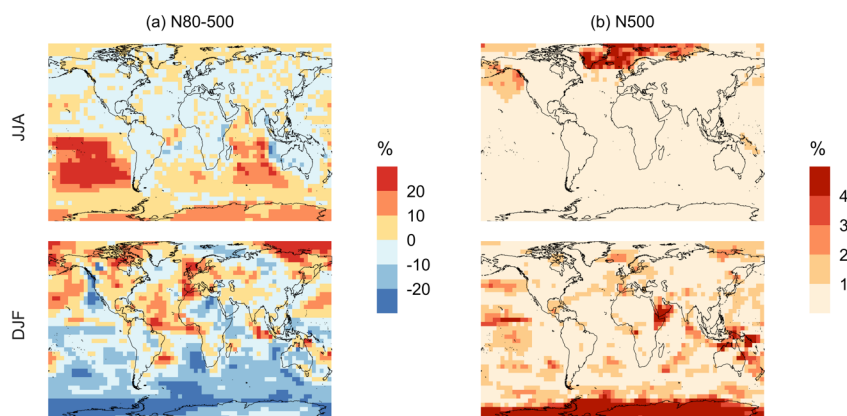
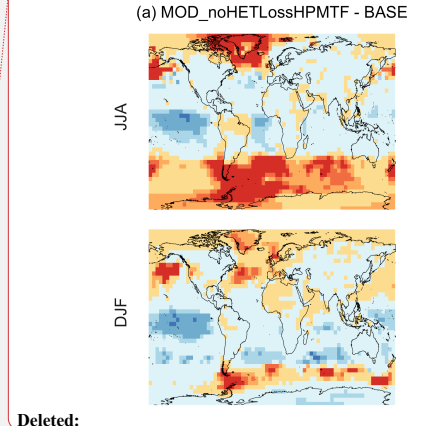
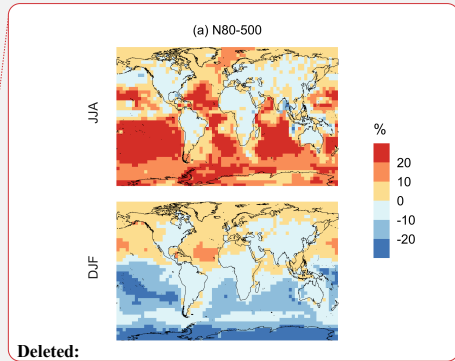


Figure A5 Geographic distribution of percent difference in seasonal-mean surface-layer aerosol number concentration in cm^{-3} for simulations similar to MOD_noHETLossHPMTF relative to simulations BASE, for particle diameters between (a) 80 – 500 nm and (b) > 500 nm. Simulations are described in Table 5.

904



Deleted:



Formatted: Superscript

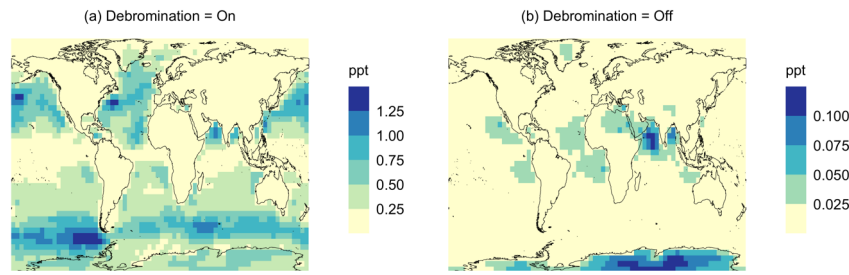
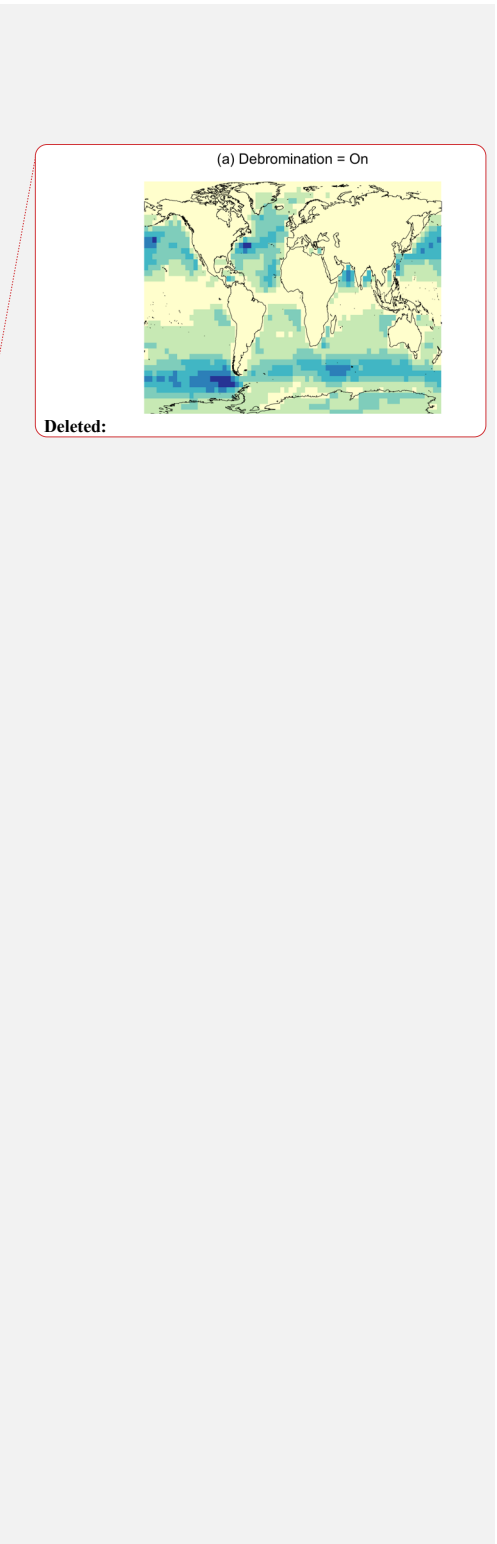


Figure A6 Geographic distribution of mean surface BrO mixing ratio (ppt) for (a) with sea salt debromination and (b) without sea salt debromination for simulation MOD. Simulations are described in Table 5.

907



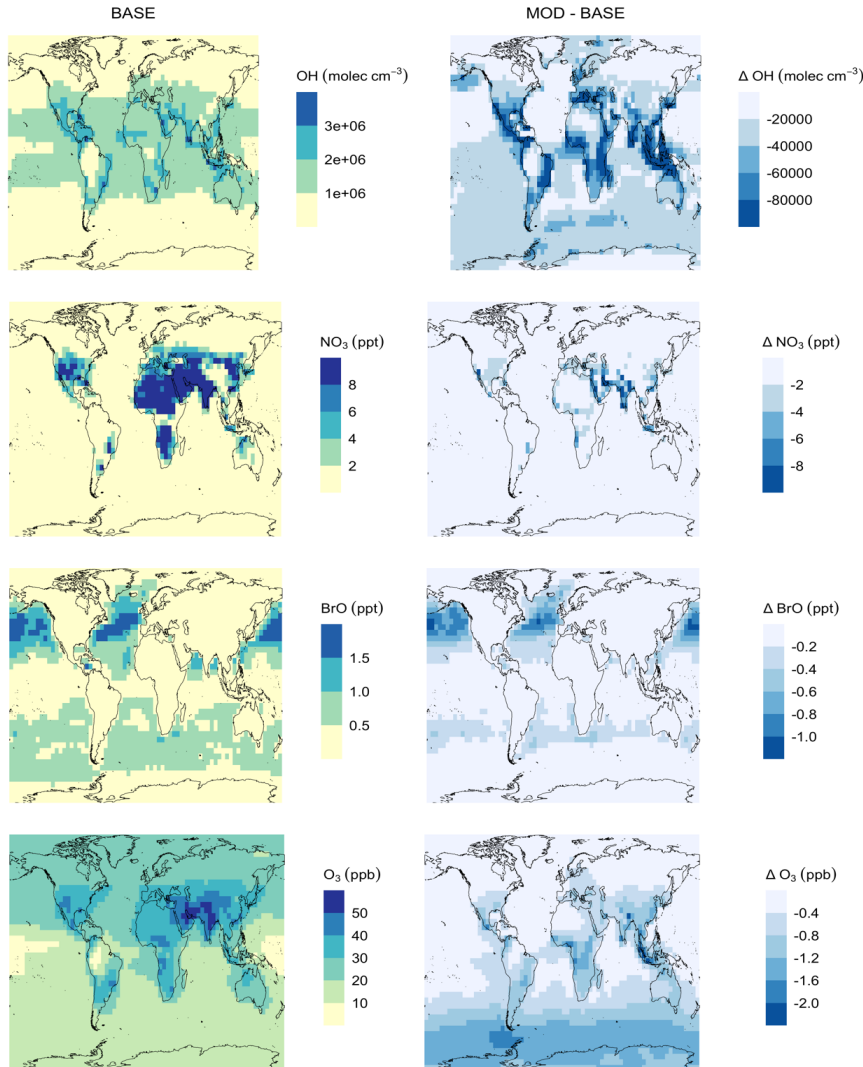


Figure A7 Geographic distribution of mean surface oxidant concentrations for simulation (a) BASE and (b) MOD - BASE. Simulations are described in Table 5.

910 **Appendix B: Additional Table**911 **Table B1.** Global atmospheric flux, deposition, burdens, lifetime of DMS and its oxidation
912 products, chemical loss rates for specific reaction pathways and global mean concentration of
913 major oxidants are listed here for the case of simulation MOD. Note that SO₂ and SO₄²⁻ includes
914 natural as well as anthropogenic sources.

F_{DMS} (Gg S yr ⁻¹)	2.2×10^4	Deleted: x
Deposition of MSA (Gg S yr ⁻¹)	3.6×10^3	Deleted: x
Deposition of HPMTF (Gg S yr ⁻¹)	9.1×10^1	Deleted: x
Deposition of DMSO (Gg S yr ⁻¹)	1.7×10^3	Deleted: x
Deposition of MSIA (Gg S yr ⁻¹)	2.1×10^2	Deleted: x
DMS (GgS)	<u>65</u>	Formatted
MSA (GgS)	<u>9.2</u>	Deleted: x
HPMTF (GgS)	<u>0.6</u>	Formatted
SO ₂ (GgS)	<u>256.7</u>	Deleted: 2 x
SO ₄ ²⁻ (GgS)	<u>612.4</u>	Deleted: 67
τ_{DMS} (d)	<u>0.9</u>	Deleted: 8.5
τ_{MSA} (d)	<u>0.9</u>	Deleted: 75
τ_{HPMTF} (d)	<u>0.6</u>	Deleted: 261.5
τ_{SO_2} (d)	<u>1.3</u>	Deleted: 598.6
$\tau_{\text{SO}_4^{2-}}$ (d)	<u>4.4</u>	Deleted: 1.
DMS lost to MSA (Gg S yr ⁻¹)	4.3×10^3	Deleted: 8
DMS lost to HPMTF (Gg S yr ⁻¹)	6.9×10^3	Deleted: 7
DMS lost to SO ₂ (Gg S yr ⁻¹)	9.5×10^3	Deleted: 1 x
MSA lost to particle growth (Gg S yr ⁻¹)	4.5×10^2	Deleted: 7.
HPMTF lost to SO ₂ (Gg S yr ⁻¹)	4.8×10^2	Deleted: x
HPMTF lost to cloud (Gg S yr ⁻¹)	6.7×10^3	Deleted: 2 x
HPMTF lost to particle growth (Gg S yr ⁻¹)	2.8×10^2	Deleted: 3 x
OH (molec cm ⁻³)	<u>8.0×10^5</u>	Deleted: 5 x
NO ₃ (ppt)	<u>0.97</u>	Deleted: x
O ₃ (ppb)	<u>21.10</u>	Deleted: 7 x
BrO (ppt)	<u>0.31</u>	Deleted: 1.1 x 10 ⁶
		Deleted: Cl (molec cm ⁻³)
		Deleted: molec cm ⁻³ (... [22])
		Deleted: 2.
		Deleted: x 10 ¹²
		Deleted: molec cm ⁻³
		Deleted: 4.4x 10 ¹⁶
		Deleted: molec cm ⁻³
		Deleted: 6.3 x 10 ¹¹

915
916 **Data availability.** The DMS observational data in Fig. 2 were obtained from the referenced
917 papers (Kouvarakis and Mihalopoulos, 2002; Castebrunet et al., 2009). The observations data
918 during ATom-4 are published through the Distributed Active Archive Center for Biogeochemical
919 Dynamics (DAAC) at (Novak et al., 2021; Wollesen de Jonge et al., 2021),
920 <https://doi.org/10.3334/ORNLDaac/1921> and
921 https://daac.ornl.gov/ATOM/guides/ATom_SO2_LIF_Instrument_Data.html.922 **Author contributions.** LT and WCP designed the research goals, aims, and methodology,
923 implemented the new code into GC-TOMAS. QC, BA, CHF and CDH contributed in code
924 development. All authors provided expert advice on data analysis, interpretation, and visualization.
925 LT ran model simulations, analyzed the data, created the figures, and led manuscript development
926 and editing.927 **Competing interests.** The contact authors have declared that none of the authors has any
928 competing interests.

959 **Acknowledgements.** LT and WCP gratefully acknowledge Ka Ming Fung for discussions on
960 DMS oxidation chemistry. BC thanks Rachel Y.-W. Chang for discussions on marine aerosols.

961 **Financial support.** LT and WCP was supported by NSF grant no. 2155192. QC was supported
962 by the Hong Kong Research Grants Council (Grant No. 15223221 and 15219722). BA was
963 supported by NSF AGS 2109323 and PLR 1904128. CHF was supported by NASA FINESST
964 (grant 80NSSC19K1368). CDH acknowledges funding support from NSF AGS (grant 1848372).
965 BC gratefully acknowledges research funding supported by the Ocean Frontier Institute, through
966 an award from the Canada First Research Excellence Fund. JRP was supported by the Atmospheric
967 System Research (ASR) program, part of the US Department of Energy's Office of Biological and
968 Environmental Research within the Office of Science, under grant DE-SC0021208. SI was
969 supported by Ferring Pharmaceuticals through the Extreme Environments research Laboratory,
970 École Polytechnique Fédérale de Lausanne (EPFL).

971 **References**

972 Adams, P. J. and Seinfeld, J. H.: Predicting global aerosol size distributions in general circulation
973 models, *J. Geophys. Res. Atmospheres*, 107, AAC 4-1-AAC 4-23,
974 <https://doi.org/10.1029/2001JD001010>, 2002.

975 Alexander, B., Park, R. J., Jacob, D. J., Li, Q. B., Yantosca, R. M., Savarino, J., Lee, C. C. W.,
976 and Thiemens, M. H.: Sulfate formation in sea-salt aerosols: Constraints from oxygen isotopes, *J.*
977 *Geophys. Res. Atmospheres*, 110, <https://doi.org/10.1029/2004JD005659>, 2005.

978 Alexander, B., Park, R. J., Jacob, D. J., and Gong, S.: Transition metal-catalyzed oxidation of
979 atmospheric sulfur: Global implications for the sulfur budget, *J. Geophys. Res. Atmospheres*,
980 114, <https://doi.org/10.1029/2008JD010486>, 2009.

981 Amos, H. M., Jacob, D. J., Holmes, C. D., Fisher, J. A., Wang, Q., Yantosca, R. M., Corbitt, E.
982 S., Galarneau, E., Rutter, A. P., Gustin, M. S., Steffen, A., Schauer, J. J., Graydon, J. A., Louis,
983 V. L. S., Talbot, R. W., Edgerton, E. S., Zhang, Y., and Sunderland, E. M.: Gas-particle
984 partitioning of atmospheric Hg(II) and its effect on global mercury deposition, *Atmospheric*
985 *Chem. Phys.*, 12, 591–603, <https://doi.org/10.5194/acp-12-591-2012>, 2012.

986 Atkinson, R., Baulch, D. L., Cox, R. A., Crowley, J. N., Hampson, R. F., Hynes, R. G., Jenkin,
987 M. E., Rossi, M. J., and Troe, J.: Evaluated kinetic and photochemical data for atmospheric
988 chemistry: Volume I - gas phase reactions of O_x, HO_x, NO_x and SO_x species, *Atmospheric*
989 *Chem. Phys.*, 4, 1461–1738, <https://doi.org/10.5194/acp-4-1461-2004>, 2004.

990 Bardouki, H., da Rosa, M. B., Mihalopoulos, N., Palm, W.-U., and Zetzsch, C.: Kinetics and
991 mechanism of the oxidation of dimethylsulfoxide (DMSO) and methanesulfinate (MSI⁻) by OH
992 radicals in aqueous medium, *Atmos. Environ.*, 36, 4627–4634, [https://doi.org/10.1016/S1352-2310\(02\)00460-0](https://doi.org/10.1016/S1352-2310(02)00460-0), 2002.

994 Barnes, I., Hjorth, J., and Mihalopoulos, N.: Dimethyl Sulfide and Dimethyl Sulfoxide and Their
995 Oxidation in the Atmosphere, *Chem. Rev.*, 106, 940–975, <https://doi.org/10.1021/cr020529+>,
996 2006.

Formatted: Font: Not Bold

997 Barone, S. B., Turnipseed, A. A., and Ravishankara, A. R.: Role of adducts in the atmospheric
998 oxidation of dimethyl sulfide, *Faraday Discuss.*, 100, 39, <https://doi.org/10.1039/fd9950000039>,
999 1995.

1000 Berndt, T., Scholz, W., Mentler, B., Fischer, L., Hoffmann, E. H., Tilgner, A., Hyttinen, N.,
1001 Prisle, N. L., Hansel, A., and Herrmann, H.: Fast Peroxy Radical Isomerization and OH
1002 Recycling in the Reaction of OH Radicals with Dimethyl Sulfide, *J. Phys. Chem. Lett.*, 10,
1003 6478–6483, <https://doi.org/10.1021/acs.jpclett.9b02567>, 2019.

1004 Berndt, T., Hoffmann, E. H., Tilgner, A., Stratmann, F., and Herrmann, H.: Direct sulfuric acid
1005 formation from the gas-phase oxidation of reduced-sulfur compounds, *Nat. Commun.*, 14, 4849,
1006 <https://doi.org/10.1038/s41467-023-40586-2>, 2023.

1007 Bey, I., Jacob, D. J., Yantosca, R. M., Logan, J. A., Field, B. D., Fiore, A. M., Li, Q., Liu, H. Y.,
1008 Mickley, L. J., and Schultz, M. G.: Global modeling of tropospheric chemistry with assimilated
1009 meteorology: Model description and evaluation, *J. Geophys. Res. Atmospheres*, 106, 23073–
1010 23095, <https://doi.org/10.1029/2001JD000807>, 2001.

1011 Boniface, J., Shi, Q., Li, Y. Q., Cheung, J. L., Rattigan, O. V., Davidovits, P., Worsnop, D. R.,
1012 Jayne, J. T., and Kolb, C. E.: Uptake of Gas-Phase SO₂, H₂S, and CO₂ by Aqueous Solutions, *J.*
1013 *Phys. Chem. A*, 104, 7502–7510, <https://doi.org/10.1021/jp000479h>, 2000.

1014 Borisenko, D., Kukui, A., Laverdet, G., and Le Bras, G.: Experimental Study of SO₂ Formation
1015 in the Reactions of CH₃SO Radical with NO₂ and O₃ in Relation with the Atmospheric
1016 Oxidation Mechanism of Dimethyl Sulfide, *J. Phys. Chem. A*, 107, 1155–1161,
1017 <https://doi.org/10.1021/jp021701g>, 2003.

1018 Boucher, O., Moulin, C., Belviso, S., Aumont, O., Bopp, L., Cosme, E., von Kuhlmann, R.,
1019 Lawrence, M. G., Pham, M., Reddy, M. S., Sciare, J., and Venkataraman, C.: DMS atmospheric
1020 concentrations and sulphate aerosol indirect radiative forcing: a sensitivity study to the DMS
1021 source representation and oxidation, *Atmospheric Chem. Phys.*, 3, 49–65,
1022 <https://doi.org/10.5194/acp-3-49-2003>, 2003.

1023 Bräuer, P., Tilgner, A., Wolke, R., and Herrmann, H.: Mechanism development and modelling of
1024 tropospheric multiphase halogen chemistry: The CAPRAM Halogen Module 2.0 (HM2), *J.*
1025 *Atmospheric Chem.*, 70, 19–52, <https://doi.org/10.1007/s10874-013-9249-6>, 2013.

1026 Breider, T. J., Chipperfield, M. P., Richards, N. a. D., Carslaw, K. S., Mann, G. W., and
1027 Spracklen, D. V.: Impact of BrO on dimethylsulfide in the remote marine boundary layer,
1028 *Geophys. Res. Lett.*, 37, <https://doi.org/10.1029/2009GL040868>, 2010.

1029 Burkholder, J. B., Sander, S. P., Abbatt, J. P. D., Barker, J. R., Cappa, C., Crounse, J. D., Dibble,
1030 T. S., Huie, R. E., Kolb, C. E., Kurylo, M. J., Orkin, V. L., Percival, C. J., Wilmouth, D. M., and
1031 Wine, P. H.: Chemical kinetics and photochemical data for use in atmospheric studies;
1032 evaluation number 19, 2020.

1033 Cala, B. A., Archer-Nicholls, S., Weber, J., Abraham, N. L., Griffiths, P. T., Jacob, L., Shin, Y.
1034 M., Revell, L. E., Woodhouse, M., and Archibald, A. T.: Development, intercomparison, and

Deleted: Huie, R. E., Kolb, C. E., Kurylo, M. J., Orkin, V. L., Wilmouth, D. M., and Wine, P. H.: Chemical kinetics and photochemical data for use in atmospheric studies: evaluation number 18, 2015.
Burkholder, J. B., Sander, S. P., Abbatt, J. P. D., Barker, J. R.,

1041 [evaluation of an improved mechanism for the oxidation of dimethyl sulfide in the UKCA model,](https://doi.org/10.5194/acp-23-14735-2023)
1042 [Atmospheric Chem. Phys., 23, 14735–14760, <https://doi.org/10.5194/acp-23-14735-2023>, 2023.](https://doi.org/10.5194/acp-23-14735-2023)

1043 [Campolongo, F., Saltelli, A., Jensen, N. R., Wilson, J., and Hjorth, J.: The Role of Multiphase](https://doi.org/10.1023/A:1006154618511)
1044 [Chemistry in the Oxidation of Dimethylsulphide \(DMS\). A Latitude Dependent Analysis, J.](https://doi.org/10.1023/A:1006154618511)
1045 [Atmospheric Chem., 32, 327–356, <https://doi.org/10.1023/A:1006154618511>, 1999.](https://doi.org/10.1023/A:1006154618511)

1046 Carslaw, K. S., Lee, L. A., Reddington, C. L., Pringle, K. J., Rap, A., Forster, P. M., Mann, G.
1047 W., Spracklen, D. V., Woodhouse, M. T., Regayre, L. A., and Pierce, J. R.: Large contribution of
1048 natural aerosols to uncertainty in indirect forcing, *Nature*, 503, 67–71,
1049 <https://doi.org/10.1038/nature12674>, 2013.

1050 Castebrunet, H., Martinerie, P., Genthon, C., and Cosme, E.: A three-dimensional model study of
1051 methanesulphonic acid to non sea salt sulphate ratio at mid and high-southern latitudes,
1052 [Atmospheric Chem. Phys., 9, 9449–9469, <https://doi.org/10.5194/acp-9-9449-2009>, 2009.](https://doi.org/10.5194/acp-9-9449-2009)

1053 Charlson, R. J., Lovelock, J. E., Andreae, M. O., and Warren, S. G.: Oceanic phytoplankton,
1054 atmospheric sulphur, cloud albedo and climate, *Nature*, 326, 655–661,
1055 <https://doi.org/10.1038/326655a0>, 1987.

1056 Chen, H., Ezell, M. J., Arquero, K. D., Varner, M. E., Dawson, M. L., Gerber, R. B., and
1057 Finlayson-Pitts, B. J.: New particle formation and growth from methanesulfonic acid,
1058 trimethylamine and water, *Phys. Chem. Chem. Phys.*, 17, 13699–13709,
1059 <https://doi.org/10.1039/C5CP00838G>, 2015.

1060 Chen, Q., Geng, L., Schmidt, J. A., Xie, Z., Kang, H., Dachs, J., Cole-Dai, J., Schauer, A. J.,
1061 Camp, M. G., and Alexander, B.: Isotopic constraints on the role of hypohalous acids in sulfate
1062 aerosol formation in the remote marine boundary layer, *Atmospheric Chem. Phys.*, 16, 11433–
1063 11450, <https://doi.org/10.5194/acp-16-11433-2016>, 2016.

1064 Chen, Q., Schmidt, J. A., Shah, V., Jaeglé, L., Sherwen, T., and Alexander, B.: Sulfate
1065 production by reactive bromine: Implications for the global sulfur and reactive bromine budgets,
1066 *Geophys. Res. Lett.*, 44, 7069–7078, <https://doi.org/10.1002/2017GL073812>, 2017.

1067 Chen, Q., Sherwen, T., Evans, M., and Alexander, B.: DMS oxidation and sulfur aerosol
1068 formation in the marine troposphere: a focus on reactive halogen and multiphase chemistry,
1069 [Atmospheric Chem. Phys., 18, 13617–13637, <https://doi.org/10.5194/acp-18-13617-2018>, 2018.](https://doi.org/10.5194/acp-18-13617-2018)

1070 Chin, M., Jacob, D. J., Gardner, G. M., Foreman-Fowler, M. S., Spiro, P. A., and Savoie, D. L.:
1071 A global three-dimensional model of tropospheric sulfate, *J. Geophys. Res. Atmospheres*, 101,
1072 18667–18690, <https://doi.org/10.1029/96JD01221>, 1996.

1073 Clarke, A. D., Davis, D., Kapustin, V. N., Eisele, F., Chen, G., Paluch, I., Lenschow, D., Bandy,
1074 A. R., Thornton, D., Moore, K., Mauldin, L., Tanner, D., Litchy, M., Carroll, M. A., Collins, J.,
1075 and Albercook, G.: Particle Nucleation in the Tropical Boundary Layer and Its Coupling to
1076 Marine Sulfur Sources, *Science*, 282, 89–92, 1998a.

1077 Clarke, A. D., Varner, J. L., Eisele, F., Mauldin, R. L., Tanner, D., and Litchy, M.: Particle
1078 production in the remote marine atmosphere: Cloud outflow and subsidence during ACE 1, *J.
1079 Geophys. Res. Atmospheres*, 103, 16397–16409, <https://doi.org/10.1029/97JD02987>, 1998b.

1080 Du, L., Xu, Y., Ge, M., Jia, L., Yao, L., and Wang, W.: Rate constant of the gas phase reaction
1081 of dimethyl sulfide (CH₃SCH₃) with ozone, *Chem. Phys. Lett.*, 436, 36–40,
1082 <https://doi.org/10.1016/j.cplett.2007.01.025>, 2007.

1083 Duncan Fairlie, T., Jacob, D. J., and Park, R. J.: The impact of transpacific transport of mineral
1084 dust in the United States, *Atmos. Environ.*, 41, 1251–1266,
1085 <https://doi.org/10.1016/j.atmosenv.2006.09.048>, 2007.

1086 Emerson, E. W., Hodshire, A. L., DeBolt, H. M., Bilsback, K. R., Pierce, J. R., McMeeking, G.
1087 R., and Farmer, D. K.: Revisiting particle dry deposition and its role in radiative effect estimates,
1088 *Proc. Natl. Acad. Sci.*, 117, 26076–26082, <https://doi.org/10.1073/pnas.2014761117>, 2020.

1089 Enami, S., Nakano, Y., Hashimoto, S., Kawasaki, M., Aloisio, S., and Francisco, J. S.: Reactions
1090 of Cl Atoms with Dimethyl Sulfide: A Theoretical Calculation and an Experimental Study with
1091 Cavity Ring-Down Spectroscopy, *J. Phys. Chem. A*, 108, 7785–7789,
1092 <https://doi.org/10.1021/jp049772y>, 2004.

1093 Faloona, I.: Sulfur processing in the marine atmospheric boundary layer: A review and critical
1094 assessment of modeling uncertainties, *Atmos. Environ.*, 43, 2841–2854,
1095 <https://doi.org/10.1016/j.atmosenv.2009.02.043>, 2009.

1096 Flyunt, R., Makagon, O., Schuchmann, M. N., Asmus, K.-D., and Sonntag, C. von: OH-Radical-
1097 induced oxidation of methanesulfenic acid. The reactions of the methanesulfonyl radical in the
1098 absence and presence of dioxygen, *J. Chem. Soc. Perkin Trans. 2*, 787–792,
1099 <https://doi.org/10.1039/B009631H>, 2001.

1100 Fung, K. M., Heald, C. L., Kroll, J. H., Wang, S., Jo, D. S., Gettelman, A., Lu, Z., Liu, X.,
1101 Zaveri, R. A., Apel, E. C., Blake, D. R., Jimenez, J.-L., Campuzano-Jost, P., Veres, P. R., Bates,
1102 T. S., Shilling, J. E., and Zawadowicz, M.: Exploring dimethyl sulfide (DMS) oxidation and
1103 implications for global aerosol radiative forcing, *Atmospheric Chem. Phys.*, 22, 1549–1573,
1104 <https://doi.org/10.5194/acp-22-1549-2022>, 2022.

1105 Galí, M., Levasseur, M., Devred, E., Simó, R., and Babin, M.: Sea-surface dimethylsulfide
1106 (DMS) concentration from satellite data at global and regional scales, *Biogeosciences*, 15, 3497–
1107 3519, <https://doi.org/10.5194/bg-15-3497-2018>, 2018.

1108 Galí, M., Devred, E., Babin, M., and Levasseur, M.: Decadal increase in Arctic dimethylsulfide
1109 emission, *Proc. Natl. Acad. Sci.*, 116, 19311–19317, <https://doi.org/10.1073/pnas.1904378116>,
1110 2019.

1111 Gershenzon, M., Davidovits, P., Jayne, J. T., Kolb, C. E., and Worsnop, D. R.: Simultaneous
1112 Uptake of DMS and Ozone on Water, *J. Phys. Chem. A*, 105, 7031–7036,
1113 <https://doi.org/10.1021/jp010696y>, 2001.

1114 von Glasow, R. and Crutzen, P. J.: Model study of multiphase DMS oxidation with a focus on
1115 halogens, *Atmospheric Chem. Phys.*, 4, 589–608, <https://doi.org/10.5194/acp-4-589-2004>, 2004.

1116 [Herrmann, H., Zellner, R., Mirabel, P., Buxton, G., Salmon, A., Sehested, K., Holcman, J., and](#)
1117 [Brede, O.: Removal and interconversions of oxidants in the atmospheric aqueous phase, part 2](#)
1118 [\(RINOXA 2\). Final report, Universität GH Essen. Institut für Physikalische und Theoretische](#)
1119 [Chemie, Essen, 1998.](#)

1120 Hezel, P. J., Alexander, B., Bitz, C. M., Steig, E. J., Holmes, C. D., Yang, X., and Sciare, J.:
1121 Modeled methanesulfonic acid (MSA) deposition in Antarctica and its relationship to sea ice, *J.*
1122 *Geophys. Res. Atmospheres*, 116, <https://doi.org/10.1029/2011JD016383>, 2011.

1123 Hodshire, A. L., Campuzano-Jost, P., Kodros, J. K., Croft, B., Nault, B. A., Schroder, J. C.,
1124 Jimenez, J. L., and Pierce, J. R.: The potential role of methanesulfonic acid (MSA) in aerosol
1125 formation and growth and the associated radiative forcings, *Atmospheric Chem. Phys.*, 19,
1126 3137–3160, <https://doi.org/10.5194/acp-19-3137-2019>, 2019.

1127 Hoffmann, E. H., Tilgner, A., Schrödner, R., Bräuer, P., Wolke, R., and Herrmann, H.: An
1128 advanced modeling study on the impacts and atmospheric implications of multiphase dimethyl
1129 sulfide chemistry, *Proc. Natl. Acad. Sci.*, 113, 11776–11781,
1130 <https://doi.org/10.1073/pnas.1606320113>, 2016.

1131 Hoffmann, E. H., Heinold, B., Kubin, A., Tegen, I., and Herrmann, H.: The Importance of the
1132 Representation of DMS Oxidation in Global Chemistry-Climate Simulations, *Geophys. Res.*
1133 *Lett.*, 48, e2021GL094068, <https://doi.org/10.1029/2021GL094068>, 2021.

1134 Holmes, C. D., Bertram, T. H., Confer, K. L., Graham, K. A., Ronan, A. C., Wirks, C. K., and
1135 Shah, V.: The Role of Clouds in the Tropospheric NO_x Cycle: A New Modeling Approach for
1136 Cloud Chemistry and Its Global Implications, *Geophys. Res. Lett.*, 46, 4980–4990,
1137 <https://doi.org/10.1029/2019GL081990>, 2019.

1138 Hoyle, C. R., Fuchs, C., Järvinen, E., Saathoff, H., Dias, A., El Haddad, I., Gysel, M., Coburn, S.
1139 C., Tröstl, J., Bernhammer, A.-K., Bianchi, F., Breitenlechner, M., Corbin, J. C., Craven, J.,
1140 Donahue, N. M., Duplissy, J., Ehrhart, S., Frege, C., Gordon, H., Höppel, N., Heinritzi, M.,
1141 Kristensen, T. B., Molteni, U., Nichman, L., Pinterich, T., Prévôt, A. S. H., Simon, M., Slowik,
1142 J. G., Steiner, G., Tomé, A., Vogel, A. L., Volkamer, R., Wagner, A. C., Wagner, R., Wexler, A.
1143 S., Williamson, C., Winkler, P. M., Yan, C., Amorim, A., Dommen, J., Curtius, J., Gallagher, M.
1144 W., Flagan, R. C., Hansel, A., Kirkby, J., Kulmala, M., Möhler, O., Stratmann, F., Worsnop, D.
1145 R., and Baltensperger, U.: Aqueous phase oxidation of sulphur dioxide by ozone in cloud
1146 droplets, *Atmospheric Chem. Phys.*, 16, 1693–1712, <https://doi.org/10.5194/acp-16-1693-2016>,
1147 2016.

1148 Ishino, S., Hattori, S., Legrand, M., Chen, Q., Alexander, B., Shao, J., Huang, J., Jaeglé, L.,
1149 Jourdain, B., Preunkert, S., Yamada, A., Yoshida, N., and Savarino, J.: Regional Characteristics
1150 of Atmospheric Sulfate Formation in East Antarctica Imprinted on ¹⁷O-Excess Signature, *J.*
1151 *Geophys. Res. Atmospheres*, 126, e2020JD033583, <https://doi.org/10.1029/2020JD033583>,
1152 2021.

1153 Jacob, D. J., Field, B. D., Li, Q., Blake, D. R., de Gouw, J., Warneke, C., Hansel, A., Wisthaler,
1154 A., Singh, H. B., and Guenther, A.: Global budget of methanol: Constraints from atmospheric
1155 observations, *J. Geophys. Res. Atmospheres*, 110, <https://doi.org/10.1029/2004JD005172>, 2005.

1156 Jernigan, C. M., Fite, C. H., Vereecken, L., Berkelhammer, M. B., Rollins, A. W., Rickly, P. S.,
1157 Novelli, A., Taraborrelli, D., Holmes, C. D., and Bertram, T. H.: Efficient Production of
1158 Carbonyl Sulfide in the Low-NO_x Oxidation of Dimethyl Sulfide, *Geophys. Res. Lett.*, 49,
1159 e2021GL096838, <https://doi.org/10.1029/2021GL096838>, 2022a.

1160 Jernigan, C. M., Cappa, C. D., and Bertram, T. H.: Reactive Uptake of Hydroperoxymethyl
1161 Thioformate to Sodium Chloride and Sodium Iodide Aerosol Particles, *J. Phys. Chem. A*, 126,
1162 4476–4481, <https://doi.org/10.1021/acs.jpca.2c03222>, 2022b.

1163 Johnson, J. S. and Jen, C. N.: Role of Methanesulfonic Acid in Sulfuric Acid–Amine and
1164 Ammonia New Particle Formation, *ACS Earth Space Chem.*, 7, 653–660,
1165 <https://doi.org/10.1021/acsearthspacechem.3c00017>, 2023.

1166 Johnson, M. T.: A numerical scheme to calculate temperature and salinity dependent air-water
1167 transfer velocities for any gas, *Ocean Sci.*, 6, 913–932, <https://doi.org/10.5194/os-6-913-2010>,
1168 2010.

1169 Kaufman, Y. J. and Tanré, D.: Effect of variations in super-saturation on the formation of cloud
1170 condensation nuclei, *Nature*, 369, 45–48, <https://doi.org/10.1038/369045a0>, 1994.

1171 Khan, M. A. H., Gillespie, S. M. P., Razis, B., Xiao, P., Davies-Coleman, M. T., Percival, C. J.,
1172 Derwent, R. G., Dyke, J. M., Ghosh, M. V., Lee, E. P. F., and Shallcross, D. E.: A modelling
1173 study of the atmospheric chemistry of DMS using the global model, STOCHEM-CRI, *Atmos.*
1174 *Environ.*, 127, 69–79, <https://doi.org/10.1016/j.atmosenv.2015.12.028>, 2016.

1175 Khan, M. A. H., Bannan, T. J., Holland, R., Shallcross, D. E., Archibald, A. T., Matthews, E.,
1176 Back, A., Allan, J., Coe, H., Artaxo, P., and Percival, C. J.: Impacts of Hydroperoxymethyl
1177 Thioformate on the Global Marine Sulfur Budget, *ACS Earth Space Chem.*, 5, 2577–2586,
1178 <https://doi.org/10.1021/acsearthspacechem.1c00218>, 2021.

1179 Kloster, S., Feichter, J., Maier-Reimer, E., Six, K. D., Stier, P., and Wetzel, P.: DMS cycle in the
1180 marine ocean-atmosphere system — a global model study, *Biogeosciences*, 3, 29–51,
1181 <https://doi.org/10.5194/bg-3-29-2006>, 2006.

1182 Kodros, J. K. and Pierce, J. R.: Important global and regional differences in aerosol cloud-albedo
1183 effect estimates between simulations with and without prognostic aerosol microphysics, *J.*
1184 *Geophys. Res. Atmospheres*, 122, 4003–4018, <https://doi.org/10.1002/2016JD025886>, 2017.

1185 Kodros, J. K., Cucinotta, R., Ridley, D. A., Wiedinmyer, C., and Pierce, J. R.: The aerosol
1186 radiative effects of uncontrolled combustion of domestic waste, *Atmospheric Chem. Phys.*, 16,
1187 6771–6784, <https://doi.org/10.5194/acp-16-6771-2016>, 2016.

1188 Kouvarakis, G. and Mihalopoulos, N.: Seasonal variation of dimethylsulfide in the gas phase and
1189 of methanesulfonate and non-sea-salt sulfate in the aerosols phase in the Eastern Mediterranean

1190 atmosphere, *Atmos. Environ.*, 36, 929–938, [https://doi.org/10.1016/S1352-2310\(01\)00511-8](https://doi.org/10.1016/S1352-2310(01)00511-8),
1191 2002.

1192 Kowalcuk, P., Cooper, W. J., Whitehead, R. F., Durako, M. J., and Sheldon, W.:
1193 Characterization of CDOM in an organic-rich river and surrounding coastal ocean in the South
1194 Atlantic Bight, *Aquat. Sci.*, 65, 384–401, <https://doi.org/10.1007/s00027-003-0678-1>, 2003.

1195 Kulmala, M.: How Particles Nucleate and Grow, *Science*, 302, 1000–1001,
1196 <https://doi.org/10.1126/science.1090848>, 2003.

1197 Kulmala, M., Pirjola, L., and Mäkelä, J. M.: Stable sulphate clusters as a source of new
1198 atmospheric particles, *Nature*, 404, 66–69, <https://doi.org/10.1038/35003550>, 2000.

1199 Lana, A., Bell, T. G., Simó, R., Vallina, S. M., Ballabrera-Poy, J., Kettle, A. J., Dachs, J., Bopp,
1200 L., Saltzman, E. S., Stefels, J., Johnson, J. E., and Liss, P. S.: An updated climatology of surface
1201 dimethylsulfide concentrations and emission fluxes in the global ocean, *Glob. Biogeochem.*
1202 Cycles

1203 Cycles, 25, <https://doi.org/10.1029/2010GB003850>, 2011.

1204 Leaitch, W. R., Sharma, S., Huang, L., Toom-Sauntry, D., Chivulescu, A., Macdonald, A. M.,
1205 von Salzen, K., Pierce, J. R., Bertram, A. K., Schroder, J. C., Shantz, N. C., Chang, R. Y.-W.,
1206 and Norman, A.-L.: Dimethyl sulfide control of the clean summertime Arctic aerosol and cloud,
1207 *Elem. Sci. Anthr.*, 1, 000017, <https://doi.org/10.12952/journal.elementa.000017>, 2013.

1208 Lee, Y. H. and Adams, P. J.: A Fast and Efficient Version of the TwO-Moment Aerosol
1209 Sectional (TOMAS) Global Aerosol Microphysics Model, *Aerosol Sci. Technol.*, 46, 678–689,
1210 <https://doi.org/10.1080/02786826.2011.643259>, 2012.

1211 Lee, Y. H., Pierce, J. R., and Adams, P. J.: Representation of nucleation mode microphysics in a
1212 global aerosol model with sectional microphysics, *Geosci. Model Dev.*, 6, 1221–1232,
1213 <https://doi.org/10.5194/gmd-6-1221-2013>, 2013.

1214 Lennartz, S. T., Krysztofiak, G., Marandino, C. A., Sinnhuber, B.-M., Tegtmeier, S., Ziska, F.,
1215 Hossaini, R., Krüger, K., Montzka, S. A., Atlas, E., Oram, D. E., Keber, T., Bönisch, H., and
1216 Quack, B.: Modelling marine emissions and atmospheric distributions of halocarbons and
1217 dimethyl sulfide: the influence of prescribed water concentration vs. prescribed emissions,
1218 *Atmospheric Chem. Phys.*, 15, 11753–11772, <https://doi.org/10.5194/acp-15-11753-2015>, 2015.

1219 Liu, H., Jacob, D. J., Bey, I., and Yantosca, R. M.: Constraints from ^{210}Pb and ^{7}Be on wet
1220 deposition and transport in a global three-dimensional chemical tracer model driven by
1221 assimilated meteorological fields, *J. Geophys. Res. Atmospheres*, 106, 12109–12128,
1222 <https://doi.org/10.1029/2000JD900839>, 2001.

1223 Lucas, D. D. and Prinn, R. G.: Mechanistic studies of dimethylsulfide oxidation products using
1224 an observationally constrained model, *J. Geophys. Res. Atmospheres*, 107, ACH 12-1-ACH 12-
1225 26, <https://doi.org/10.1029/2001JD000843>, 2002.

1225 Napari, I., Noppel, M., Vehkämäki, H., and Kulmala, M.: Parametrization of ternary nucleation
1226 rates for H₂SO₄-NH₃-H₂O vapors, *J. Geophys. Res. Atmospheres*, 107, AAC 6-1-AAC 6-6,
1227 <https://doi.org/10.1029/2002JD002132>, 2002.

1228 Nightingale, P. D., Malin, G., Law, C. S., Watson, A. J., Liss, P. S., Liddicoat, M. I., Boutin, J.,
1229 and Upstill-Goddard, R. C.: In situ evaluation of air-sea gas exchange parameterizations using
1230 novel conservative and volatile tracers, *Glob. Biogeochem. Cycles*, 14, 373–387,
1231 <https://doi.org/10.1029/1999GB900091>, 2000.

1232 Novak, G. A., Fite, C. H., Holmes, C. D., Veres, P. R., Neuman, J. A., Faloona, I., Thornton, J.
1233 A., Wolfe, G. M., Vermeuel, M. P., Jernigan, C. M., Peischl, J., Ryerson, T. B., Thompson, C.
1234 R., Bourgeois, I., Warneke, C., Gkatzelis, G. I., Coggon, M. M., Sekimoto, K., Bui, T. P., Dean-
1235 Day, J., Diskin, G. S., DiGangi, J. P., Nowak, J. B., Moore, R. H., Wiggins, E. B., Winstead, E.
1236 L., Robinson, C., Thornhill, K. L., Sanchez, K. J., Hall, S. R., Ullmann, K., Dollner, M.,
1237 Weinzierl, B., Blake, D. R., and Bertram, T. H.: Rapid cloud removal of dimethyl sulfide
1238 oxidation products limits SO₂ and cloud condensation nuclei production in the marine
1239 atmosphere, *Proc. Natl. Acad. Sci.*, 118, e2110472118,
1240 <https://doi.org/10.1073/pnas.2110472118>, 2021.

1241 Novak, G. A., Kilgour, D. B., Jernigan, C. M., Vermeuel, M. P., and Bertram, T. H.: Oceanic
1242 emissions of dimethyl sulfide and methanethiol and their contribution to sulfur dioxide
1243 production in the marine atmosphere, *Atmospheric Chem. Phys.*, 22, 6309–6325,
1244 <https://doi.org/10.5194/acp-22-6309-2022>, 2022.

1245 Park, R. J., Jacob, D. J., Field, B. D., Yantosca, R. M., and Chin, M.: Natural and transboundary
1246 pollution influences on sulfate-nitrate-ammonium aerosols in the United States: Implications for
1247 policy, *J. Geophys. Res. Atmospheres*, 109, <https://doi.org/10.1029/2003JD004473>, 2004.

1248 Parrella, J. P., Jacob, D. J., Liang, Q., Zhang, Y., Mickley, L. J., Miller, B., Evans, M. J., Yang,
1249 X., Pyle, J. A., Theys, N., and Van Roozendael, M.: Tropospheric bromine chemistry:
1250 implications for present and pre-industrial ozone and mercury, *Atmospheric Chem. Phys.*, 12,
1251 6723–6740, <https://doi.org/10.5194/acp-12-6723-2012>, 2012.

1252 Pierce, J. R. and Adams, P. J.: Global evaluation of CCN formation by direct emission of sea salt
1253 and growth of ultrafine sea salt, *J. Geophys. Res. Atmospheres*, 111,
1254 <https://doi.org/10.1029/2005JD006186>, 2006.

1255 Pound, R. J., Sherwen, T., Helmig, D., Carpenter, L. J., and Evans, M. J.: Influences of oceanic
1256 ozone deposition on tropospheric photochemistry, *Atmospheric Chem. Phys.*, 20, 4227–4239,
1257 <https://doi.org/10.5194/acp-20-4227-2020>, 2020.

1258 Pye, H. O. T., Liao, H., Wu, S., Mickley, L. J., Jacob, D. J., Henze, D. K., and Seinfeld, J. H.:
1259 Effect of changes in climate and emissions on future sulfate-nitrate-ammonium aerosol levels in
1260 the United States, *J. Geophys. Res. Atmospheres*, 114, <https://doi.org/10.1029/2008JD010701>,
1261 2009.

1262 Rosati, B., Isokäntä, S., Christiansen, S., Jensen, M. M., Moosakutty, S. P., Wollesen de Jonge,
1263 R., Massling, A., Glasius, M., Elm, J., Virtanen, A., and Bilde, M.: Hygroscopicity and CCN

Deleted: Pham, M., Müller, J.-F., Brasseur, G. P., Granier, C., and Mégie, G.: A three-dimensional study of the tropospheric sulfur cycle, *J. Geophys. Res. Atmospheres*, 100, 26061–26092, <https://doi.org/10.1029/95JD02095>, 1995.

1269 potential of DMS-derived aerosol particles, *Atmospheric Chem. Phys.*, 22, 13449–13466,
1270 <https://doi.org/10.5194/acp-22-13449-2022>, 2022.

1271 **Deleted:** Schmidt, J. A., Jacob, D. J., Horowitz, H. M., Hu, L., Sherwen, T., Evans, M. J., Liang, Q.,
1272 Suleiman, R. M., Oram, D. E., Le Breton, M., Percival, C. J., Wang, S., Dix, B., and Volkamer,
1273 R.: Modeling the observed tropospheric BrO background: Importance of multiphase chemistry
1274 and implications for ozone, OH, and mercury, *J. Geophys. Res. Atmospheres*, 121, 11,819–
1275 11,835, <https://doi.org/10.1002/2015JD024229>, 2016.

1276 Schobesberger, S., Junninen, H., Bianchi, F., Lönn, G., Ehn, M., Lehtipalo, K., Dommen, J.,
1277 Ehrhart, S., Ortega, I. K., Franchin, A., Nieminen, T., Riccobono, F., Hutterli, M., Duplissy, J.,
1278 Almeida, J., Amorim, A., Breitenlechner, M., Downard, A. J., Dunne, E. M., Flagan, R. C.,
1279 Kajos, M., Keskinen, H., Kirkby, J., Kupec, A., Kürten, A., Kurtén, T., Laaksonen, A., Mathot, S.,
1280 Onnela, A., Praplan, A. P., Rondo, L., Santos, F. D., Schallhart, S., Schnitzhofer, R., Sipilä, M.,
1281 Tomé, A., Tsagkogeorgas, G., Vehkamäki, H., Wimmer, D., Baltensperger, U., Carslaw, K. S.,
1282 Curtius, J., Hansel, A., Petäjä, T., Kulmala, M., Donahue, N. M., and Worsnop, D. R.: Molecular
1283 understanding of atmospheric particle formation from sulfuric acid and large oxidized organic
1284 molecules, *Proc. Natl. Acad. Sci.*, 110, 17223–17228, <https://doi.org/10.1073/pnas.1306973110>,
1285 2013.

1286 **Deleted:** Sherwen, T., Schmidt, J. A., Evans, M. J., Carpenter, L. J., Großmann, K., Eastham, S. D., Jacob,
1287 D. J., Dix, B., Koenig, T. K., Sinreich, R., Ortega, I., Volkamer, R., Saiz-Lopez, A., Prados-
1288 Roman, C., Mahajan, A. S., and Ordóñez, C.: Global impacts of tropospheric halogens (Cl, Br, I)
1289 on oxidants and composition in GEOS-Chem, *Atmospheric Chem. Phys.*, 16, 12239–12271,
1290 <https://doi.org/10.5194/acp-16-12239-2016>, 2016a.

1291 Sherwen, T. M., Evans, M. J., Spracklen, D. V., Carpenter, L. J., Chance, R., Baker, A. R.,
1292 Schmidt, J. A., and Breider, T. J.: Global modeling of tropospheric iodine aerosol, *Geophys. Res.*
1293 *Lett.*, 43, 10012–10019, <https://doi.org/10.1002/2016GL070062>, 2016b.

1294 Sipilä, M., Berndt, T., Petäjä, T., Brus, D., Vanhanen, J., Stratmann, F., Patokoski, J., Mauldin,
1295 R. L., Hyvärinen, A.-P., Lihavainen, H., and Kulmala, M.: The Role of Sulfuric Acid in
1296 Atmospheric Nucleation, *Science*, 327, 1243–1246, <https://doi.org/10.1126/science.1180315>,
1297 2010.

1298 Spracklen, D. V., Pringle, K. J., Carslaw, K. S., Chipperfield, M. P., and Mann, G. W.: A global
1299 off-line model of size-resolved aerosol microphysics: I. Model development and prediction of
1300 aerosol properties, *Atmospheric Chem. Phys.*, 5, 2227–2252, <https://doi.org/10.5194/acp-5-2227-2005>, 2005.

1302 Thomas, M. A., Suntharalingam, P., Pozzoli, L., Rast, S., Devasthale, A., Kloster, S., Feichter, J.,
1303 and Lenton, T. M.: Quantification of DMS aerosol-cloud-climate interactions using the
1304 ECHAM5-HAMMOZ model in a current climate scenario, *Atmospheric Chem. Phys.*, 10, 7425–
1305 7438, <https://doi.org/10.5194/acp-10-7425-2010>, 2010.

1306 Trivitayanurak, W., Adams, P. J., Spracklen, D. V., and Carslaw, K. S.: Tropospheric aerosol
1307 microphysics simulation with assimilated meteorology: model description and intermodel

Deleted: Saunders, S. M., Jenkin, M. E., Derwent, R. G., and Pilling, M. J.: Protocol for the development of the Master Chemical Mechanism, MCM v3 (Part A): tropospheric degradation of non-aromatic volatile organic compounds, *Atmospheric Chem. Phys.*, 3, 161–180, <https://doi.org/10.5194/acp-3-161-2003>, 2003. 

Deleted: Schested, K. and Holcman, J.: A pulse radiolysis study of the OH radical induced autoxidation of methanesulfinic acid, *Radiat. Phys. Chem.*, 47, 357–360, [https://doi.org/10.1016/0969-806X\(95\)00115-E](https://doi.org/10.1016/0969-806X(95)00115-E), 1996. 

1318 comparison, Atmospheric Chem. Phys., 8, 3149–3168, <https://doi.org/10.5194/acp-8-3149-2008>,
1319 2008.

1320 [Urbanski, S. P. and Wine, P. H.: Spectroscopic and Kinetic Study of the Cl–S\(CH₃\)₂ Adduct, J.](#)
1321 [Phys. Chem. A, 103, 10935–10944, https://doi.org/10.1021/jp992682m, 1999.](#)

1322 Vehkämäki, H., Kulmala, M., Napari, I., Lehtinen, K. E. J., Timmreck, C., Noppel, M., and
1323 Laaksonen, A.: An improved parameterization for sulfuric acid–water nucleation rates for
1324 tropospheric and stratospheric conditions, J. Geophys. Res. Atmospheres, 107, AAC 3-1-AAC 3-
1325 10, <https://doi.org/10.1029/2002JD002184>, 2002.

1326 Veres, P. R., Neuman, J. A., Bertram, T. H., Assaf, E., Wolfe, G. M., Williamson, C. J.,
1327 Weinzierl, B., Tilmes, S., Thompson, C. R., Thamess, A. B., Schroder, J. C., Saiz-Lopez, A.,
1328 Rollins, A. W., Roberts, J. M., Price, D., Peischl, J., Nault, B. A., Møller, K. H., Miller, D. O.,
1329 Meinardi, S., Li, Q., Lamarque, J.-F., Kupc, A., Kjaergaard, H. G., Kinnison, D., Jimenez, J. L.,
1330 Jernigan, C. M., Hornbrook, R. S., Hills, A., Dollner, M., Day, D. A., Cuevas, C. A.,
1331 Campuzano-Jost, P., Burkholder, J., Bui, T. P., Brune, W. H., Brown, S. S., Brock, C. A.,
1332 Bourgeois, I., Blake, D. R., Apel, E. C., and Ryerson, T. B.: Global airborne sampling reveals a
1333 previously unobserved dimethyl sulfide oxidation mechanism in the marine atmosphere, Proc.
1334 Natl. Acad. Sci., 117, 4505–4510, <https://doi.org/10.1073/pnas.1919344117>, 2020.

1335 Vermeuel, M. P., Novak, G. A., Jernigan, C. M., and Bertram, T. H.: Diel Profile of
1336 Hydroperoxymethyl Thioformate: Evidence for Surface Deposition and Multiphase Chemistry,
1337 Environ. Sci. Technol., 54, 12521–12529, <https://doi.org/10.1021/acs.est.0c04323>, 2020.

1338 Wang, W.-L., Song, G., Primeau, F., Saltzman, E. S., Bell, T. G., and Moore, J. K.: Global ocean
1339 dimethyl sulfide climatology estimated from observations and an artificial neural network,
1340 Biogeosciences, 17, 5335–5354, <https://doi.org/10.5194/bg-17-5335-2020>, 2020.

1341 Wang, X., Jacob, D. J., Eastham, S. D., Sulprizio, M. P., Zhu, L., Chen, Q., Alexander, B.,
1342 Sherwen, T., Evans, M. J., Lee, B. H., Haskins, J. D., Lopez-Hilfiker, F. D., Thornton, J. A.,
1343 Huey, G. L., and Liao, H.: The role of chlorine in global tropospheric chemistry, Atmospheric
1344 Chem. Phys., 19, 3981–4003, <https://doi.org/10.5194/acp-19-3981-2019>, 2019.

1345 Wang, X., Jacob, D. J., Downs, W., Zhai, S., Zhu, L., Shah, V., Holmes, C. D., Sherwen, T.,
1346 Alexander, B., Evans, M. J., Eastham, S. D., Neuman, J. A., Veres, P. R., Koenig, T. K.,
1347 Volkamer, R., Huey, L. G., Bannan, T. J., Percival, C. J., Lee, B. H., and Thornton, J. A.: Global
1348 tropospheric halogen (Cl, Br, I) chemistry and its impact on oxidants, Atmospheric Chem. Phys.,
1349 21, 13973–13996, <https://doi.org/10.5194/acp-21-13973-2021>, 2021.

1350 Wang, Y., Jacob, D. J., and Logan, J. A.: Global simulation of tropospheric O₃-NO x -
1351 hydrocarbon chemistry: 1. Model formulation, J. Geophys. Res. Atmospheres, 103, 10713–
1352 10725, <https://doi.org/10.1029/98JD00158>, 1998.

1353 Wesely, M. L.: Parameterization of surface resistances to gaseous dry deposition in regional-
1354 scale numerical models, Atmospheric Environ. 1967, 23, 1293–1304,
1355 [https://doi.org/10.1016/0004-6981\(89\)90153-4](https://doi.org/10.1016/0004-6981(89)90153-4), 1989.

1356 Westervelt, D. M., Pierce, J. R., Riipinen, I., Trivitayanurak, W., Hamed, A., Kulmala, M.,
1357 Laaksonen, A., Decesari, S., and Adams, P. J.: Formation and growth of nucleated particles into
1358 cloud condensation nuclei: model-measurement comparison, *Atmospheric Chem. Phys.*, 13,
1359 7645–7663, <https://doi.org/10.5194/acp-13-7645-2013>, 2013.

1360 Williamson, C. J., Kupc, A., Axisa, D., Bilsback, K. R., Bui, T., Campuzano-Jost, P., Dollner,
1361 M., Froyd, K. D., Hodshire, A. L., Jimenez, J. L., Kodros, J. K., Luo, G., Murphy, D. M., Nault,
1362 B. A., Ray, E. A., Weinzierl, B., Wilson, J. C., Yu, F., Yu, P., Pierce, J. R., and Brock, C. A.: A
1363 large source of cloud condensation nuclei from new particle formation in the tropics, *Nature*,
1364 574, 399–403, <https://doi.org/10.1038/s41586-019-1638-9>, 2019.

1365 Wollesen de Jonge, R., Elm, J., Rosati, B., Christiansen, S., Hyttinen, N., Lüdemann, D., Bilde,
1366 M., and Roldin, P.: Secondary aerosol formation from dimethyl sulfide – improved mechanistic
1367 understanding based on smog chamber experiments and modelling, *Atmospheric Chem. Phys.*,
1368 21, 9955–9976, <https://doi.org/10.5194/acp-21-9955-2021>, 2021.

1369 Wu, R., Wang, S., and Wang, L.: New Mechanism for the Atmospheric Oxidation of Dimethyl
1370 Sulfide. The Importance of Intramolecular Hydrogen Shift in a CH₃SCH₂OO Radical, *J. Phys.*
1371 *Chem. A*, 119, 112–117, <https://doi.org/10.1021/jp511616j>, 2015.

1372 Zhang, J.-Z. and Millero, F. J.: The products from the oxidation of H₂S in seawater, *Geochim.*
1373 *Cosmochim. Acta*, 57, 1705–1718, [https://doi.org/10.1016/0016-7037\(93\)90108-9](https://doi.org/10.1016/0016-7037(93)90108-9), 1993.

1374 Zhang, Y., Jacob, D. J., Maasakkers, J. D., Sulprizio, M. P., Sheng, J.-X., Gautam, R., and
1375 Worden, J.: Monitoring global tropospheric OH concentrations using satellite observations of
1376 atmospheric methane, *Atmospheric Chem. Phys.*, 18, 15959–15973, <https://doi.org/10.5194/acp-18-15959-2018>, 2018.

1377 Zhou, Z.-X., Lujan, S. A., Burkholder, A. B., Garbacz, M. A., and Kunkel, T. A.: Roles for DNA
1378 polymerase δ in initiating and terminating leading strand DNA replication, *Nat. Commun.*, 10,
1379 3992, <https://doi.org/10.1038/s41467-019-11995-z>, 2019.

1380 Zhu, L., Nicovich, J. M., and Wine, P. H.: Temperature-dependent kinetics studies of aqueous
1381 phase reactions of hydroxyl radicals with dimethylsulfoxide, dimethylsulfone, and
1382 methanesulfonate, *Aquat. Sci.*, 65, 425–435, <https://doi.org/10.1007/s00027-003-0673-6>, 2003.

1383 Zhu, L., Nenes, A., Wine, P. H., and Nicovich, J. M.: Effects of aqueous organosulfur chemistry
1384 on particulate methanesulfonate to non-sea salt sulfate ratios in the marine atmosphere, *J.*
1385 *Geophys. Res. Atmospheres*, 111, <https://doi.org/10.1029/2005JD006326>, 2006.

1386 Zhu, L., Jacob, D. J., Eastham, S. D., Sulprizio, M. P., Wang, X., Sherwen, T., Evans, M. J.,
1387 Chen, Q., Alexander, B., Koenig, T. K., Volkamer, R., Huey, L. G., Le Breton, M., Bannan, T.,
1388 J., and Percival, C. J.: Effect of sea salt aerosol on tropospheric bromine chemistry, *Atmospheric*
1389 *Chem. Phys.*, 19, 6497–6507, <https://doi.org/10.5194/acp-19-6497-2019>, 2019.

1390

1391

Page 7: [1] Deleted Linia Tashmim 12/16/23 10:47:00 AM

Page 7: [1] Deleted Linia Tashmim 12/16/23 10:47:00 AM

Page 7: [2] Deleted Linia Tashmim 12/16/23 10:47:00 AM

Page 7: [2] Deleted Linia Tashmim 12/16/23 10:47:00 AM

Page 7: [2] Deleted Linia Tashmim 12/16/23 10:47:00 AM

Page 7: [3] Formatted Linia Tashmim 12/16/23 10:47:00 AM

English (US), Superscript

Page 7: [3] Formatted Linia Tashmim 12/16/23 10:47:00 AM

English (US), Superscript

Page 7: [4] Deleted Linia Tashmim 12/16/23 10:47:00 AM

Page 7: [4] Deleted Linia Tashmim 12/16/23 10:47:00 AM

Page 7: [5] Formatted Linia Tashmim 12/16/23 10:47:00 AM

Superscript

Page 7: [5] Formatted Linia Tashmim 12/16/23 10:47:00 AM

Superscript

Page 7: [6] Deleted Linia Tashmim 12/16/23 10:47:00 AM

Page 7: [6] Deleted Linia Tashmim 12/16/23 10:47:00 AM

Page 7: [6] Deleted Linia Tashmim 12/16/23 10:47:00 AM

Page 7: [7] Deleted Linia Tashmim 12/16/23 10:47:00 AM

Page 7: [7] Deleted Linia Tashmim 12/16/23 10:47:00 AM

Page 7: [7] Deleted Linia Tashmim 12/16/23 10:47:00 AM

Page 8: [8] Deleted Linia Tashmim 12/16/23 10:47:00 AM

Page 8: [8] Deleted Linia Tashmim 12/16/23 10:47:00 AM

Page 8: [9] Formatted Linia Tashmim 12/16/23 10:47:00 AM

Superscript, Highlight

Page 8: [9] Formatted Linia Tashmim 12/16/23 10:47:00 AM

Superscript, Highlight

Page 8: [10] Formatted Linia Tashmim 12/16/23 10:47:00 AM

Superscript, Highlight

Page 8: [11] Deleted Linia Tashmim 12/16/23 10:47:00 AM

Page 8: [11] Deleted Linia Tashmim 12/16/23 10:47:00 AM

Page 8: [12] Formatted Linia Tashmim 12/16/23 10:47:00 AM

Superscript

Page 8: [12] Formatted Linia Tashmim 12/16/23 10:47:00 AM

Superscript

Page 8: [13] Formatted Linia Tashmim 12/16/23 10:47:00 AM

Superscript

Page 8: [13] Formatted Linia Tashmim 12/16/23 10:47:00 AM

Superscript

Page 8: [14] Formatted Linia Tashmim 12/16/23 10:47:00 AM

Not Highlight

Page 8: [15] Formatted Linia Tashmim 12/16/23 10:47:00 AM

Superscript

Page 8: [15] Formatted Linia Tashmim 12/16/23 10:47:00 AM

Superscript

Page 8: [16] Formatted Linia Tashmim 12/16/23 10:47:00 AM

English (US), Superscript

Page 8: [16] Formatted Linia Tashmim 12/16/23 10:47:00 AM

English (US), Superscript

Page 8: [17] Deleted Linia Tashmim 12/16/23 10:47:00 AM

Page 8: [18] Formatted Linia Tashmim 12/16/23 10:47:00 AM

Formatted

Page 8: [19] Formatted Linia Tashmim 12/16/23 10:47:00 AM

, Highlight

Page 8: [20] Formatted Linia Tashmim 12/16/23 10:47:00 AM

Superscript

Page 8: [21] Formatted Linia Tashmim 12/16/23 10:47:00 AM

Superscript

Page 29: [22] Deleted Linia Tashmim 12/16/23 10:47:00 AM